HHS Public Access

Author manuscript

J Am Chem Soc. Author manuscript; available in PMC 2024 July 01.

Published in final edited form as:

J Am Chem Soc. 2024 May 22; 146(20): 13817–13835. doi:10.1021/jacs.3c14346.

Identification, Characterization, and Electronic Structures of Interconvertible Cobalt-Oxygen TAML Intermediates

Deesha D. Malik[†], **Wooyeol Ryu**[‡], **Yujeong Kim**[§], **Gurjot Singh**[#], **Jun-Hyeong Kim**[‡,¶], **Muniyandi Sankaralingam**[†], **Yong-Min Lee**[†], **Mi Sook Seo**[†], **Mahesh Sundararajan**[‡,¶,Δ], **Daniel Ocampo**[‖], **Michael Roemelt**[#], **Kiyoung Park**[‡], **Sun Hee Kim**[§,⊥], **Mu-Hyun Baik**[‡,¶], **Jason Shearer**[‖], **Kallol Ray**[#], **Shunichi Fukuzumi**[†], **Wonwoo Nam**[†,±]

[†]Department of Chemistry and Nano Science, Ewha Womans University, Seoul 03760, Korea

[‡]Department of Chemistry, Korea Advanced Institute of Science and Technology, Daejeon 34141, Korea

[§]Western Seoul Center, Korea Basic Science Institute, Seoul 03759, Korea

[#]Department of Chemistry, Humboldt-Universität zu Berlin, Brook-Taylor-Straße 2, 12489 Berlin, Germany

[¶]Center for Catalytic Hydrocarbon Functionalizations, Institute for Basic Science, Daejeon 34141, Korea

[Δ]Theoretical Chemistry Section, Chemistry Division, Bhabha Atomic Research Centre, Mumbai–400 085, India

[‖]Department of Chemistry, Trinity University, San Antonio, Texas 78212-7200, United States

[⊥]Department of Chemistry, Chung-Ang University, Seoul 06974, Korea

[±]State Key Laboratory for Oxo Synthesis and Selective Oxidation, Lanzhou Institute of Chemical Physics, Chinese Academy of Sciences, Lanzhou 730000, China

Abstract

The reaction of Li[(TAML)Co^{III}]•3H_2O (TAML = tetraamido macrocyclic tetraanionic ligand) with iodosylbenzene at 253 K in acetone in the presence of redox-innocent metal ions ($Sc(OTf)_3$ and $Y(OTf)_3$) or triflic acid affords a blue species **1**, which is converted reversibly to a green species **2** upon cooling to 193 K. The electronic structures of **1** and **2** have been determined by combining advanced spectroscopic techniques (X-band EPR, ENDOR, XAS/EXAFS, and MCD) with *ab initio* theoretical studies. Complex **1** is best represented as an $S = 1/2$ [(Sol)($TAML^{\bullet+}$)Co^{III}---OH(LA)]$^-$ species (LA = Lewis/Brønsted acid and Sol = solvent), where an

Corresponding Authors: wwnam@ewha.ac.kr, fukuzumi@chem.eng.osaka-u.ac.jp, kallol.ray@cms.hu-berlin.de, jshearer@trinity.edu, mbaik2805@kaist.ac.kr, shkim7@kbsi.re.kr, kiyoung.park@kaist.ac.kr, michael.roemelt@hu-berlin.de.

ASSOCIATED CONTENT

Supporting Information. The Supporting Information is available free of charge via the Internet at http://pubs.acs.org. Structural and spectroscopic characterization of **1** and **2** by UV-vis (Figures S1, S2, S23 – S26 and Tables S1, S2), EPR (Figures S3 – S9, S22, S23 and S27-S30), CSI-MS (Figure S6), ESI-MS (Figures S22, S23 and S27-S30) rRaman (Figure S15), EXAFS (Tables S3 – S5), DFT (Tables S6 and S5 and Figures S16 – S18), MCD (Tables S8 – S10 and Figures S10 – S14) Kinetics (Figures S19, S20, S21-S24) and GC-MS (Figures S22 and S23) (PDF).

$S = 1$ Co(III) center is antiferromagnetically coupled to $S = 1/2$ TAML$^{\bullet+}$, which represents a one-electron oxidized TAML ligand. In contrast, complex **2**, also with an $S = 1/2$ ground state, is found to be multiconfigurational with contributions of both the resonance forms [(H-TAML)Co^{IV}=O(LA)]$^{-}$ and [(H-TAML$^{\bullet+}$)Co^{III}=O(LA)]$^{-}$; H-TAML and H-TAML$^{\bullet+}$ represent the protonated forms of TAML and TAML$^{\bullet+}$ ligands, respectively. Thus, the interconversion of **1** and **2** is associated with a LA-associated tautomerization event, whereby H^+ shifts from the terminal -OH group to TAML$^{\bullet+}$ with the concomitant formation of a terminal cobalt-oxo species possessing both singlet ($S_{Co} = 0$) Co(III) and doublet ($S_{Co} = 1/2$) Co(IV) characters. The reactivities of **1** and **2** at different temperatures have been investigated in oxygen transfer (OAT) and hydrogen atom transfer (HAT) reactions to compare the activation enthalpies and entropies of **1** and **2**.

Graphical Abstract

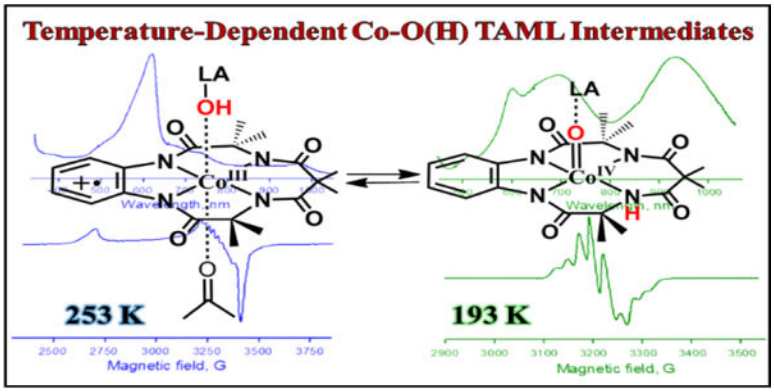

INTRODUCTION

The intimate knowledge of the mechanism by which a homogeneous catalyst operates is crucial to improve the catalyst's performance through rational modification. In our continuous efforts towards achieving carbon-free energy sources, in particular in the context of catalytic water splitting schemes,[1–35] the knowledge of how archetypical ligands based on oxygen bound at the metal center, such as oxo, hydroxo, superoxo, and (hydro)peroxo, are transformed within a transition metal's coordination sphere can provide basic knowledge concerning these fundamental transformations.

Recently, several reports have detailed the effectiveness of molecular cobalt complexes as catalysts for water-splitting reactions.[36–50] Although the homogeneity of these reactions has been convincingly established in many cases,[51–55] the harshness of the reaction conditions and the transient nature of some intermediates made it challenging to establish the structural properties of the species involved along the catalytic pathway, which resulted in an ambiguous reaction mechanism.[36–50] The interconversion between cobalt-oxo and cobalt-hydroxo species[56–58] are particularly relevant for their proposed role in artificial water oxidation. However, there is a lack of direct evidence for either of these species under catalytic turnover reaction conditions. Electronic structures and reactivities of molecular complexes containing Co-oxo/hydroxo cores can also provide detailed mechanistic insights. However, examples of well-characterized molecular cobalt-oxo cores are rare, presumably

because of their electronic instability in tetragonal symmetry. This phenomenon is known as the “oxo wall”.[59–64] Similarly, the generation of cobalt-hydroxide cores is hampered by the inherent instability of the terminal hydroxide complexes against the formation of oxo-bridged clusters.

In recent years, a few cobalt-oxo complexes stable enough for spectroscopic characterization have been successfully synthesized by employing non-tetragonal fields and/or by utilizing the stabilizing interaction provided by Lewis or Brønsted acids (Scheme 1). As far as high-valent Co(IV)-oxo complexes are concerned, $[(13\text{-TMC})Co^{IV}(O)]^{2+}$ (13-TMC = 1,4,7,10-tetramethyl-1,4,7,10-tetraazacyclotridecane)[65] and $[(12\text{-TBC})Co^{IV}(O)]^{2+}$ (12-TBC = 1,4,7,10-tetrabenzyl-1,4,7,10-tetraazacyclododecane)[66] constitute the best characterized terminal Co(IV)–oxo complexes to date, which are both stabilized by secondary interactions provided by Brønsted acid. However, the proposed role of Lewis acids in the stabilization of Co^{IV}-oxo cores is still ambiguous. In 2011, $[(TMG_3tren)Co^{IV}(O)]^{2+}$–$Sc^{3+}$ (TMG_3tren = tris[2-(*N*-tetramethylguanidyl)ethyl]amine) was reported by one of us and proposed to contain an $S = 3/2$ Co^{IV}-O motif based on electron paramagnetic resonance (EPR), X-ray absorption spectroscopy (XAS), extended X-ray absorption fine structure (EXAFS), and density functional theory (DFT) calculations.[67] Later, Borovik and co-workers synthesized a $[(MST)Co^{III}(\mu\text{-}OH)]^{2+}$–$Ca^{2+}$ {MST =*N*,*N*′,*N*″-[2,2′,2″-nitrilotris(ethane-2,1-diyl)]tris(2,4,6-trimethylbenzenesulfonamido)} complex[68] and observed that its geometric and spectroscopic properties are similar to those previously reported for $[(TMG_3tren)Co^{IV}(O)]^{2+}$–$Sc^{3+}$;[67] accordingly, an alternative $[(TMG_3tren)Co^{III}(OH)]^{+}$–$Sc^{3+}$ assignment was suggested with a hydroxide ligand bridging the cobalt and scandium centers. A $[(TAML)Co^{IV}(O)]^{2-}$–Sc^{3+} (TAML = tetraamido macrocyclic tetraanionic ligand) complex was also reported to contain a Co^{IV}–O core based on XAS/EXAFS analyses.[69,70] However, since the TAML ligand is non-innocent as demonstrated by Collins and others,[71–75] questions remained with respect to the actual presence of a Co(IV) center in this complex. Furthermore, the EPR spectrum of $[(TAML)Co^{IV}(O)]^{2-}$–Sc^{3+} proved to be ambiguous. We initially assigned a highly rhombic signal with $g_x = 2.57$, $g_y = 2.16$, and $g_z = 2.03$ to $[(TAML)Co^{IV}(O)]^{2-}$–Sc^{3+}. However, based on further studies, we concluded that $[(TAML)Co^{IV}(O)]^{2-}$–Sc^{3+} rather exhibits an isotropic signal at $g \approx 2.0$ at 5K. This is, nevertheless, inconsistent with the expected rhombic/axial signal with a significant deviation from $g \approx 2.0$ for an $S = 1/2$ Co(IV) center containing a metal-based radical,[69,70,76,77] and the origin of the initially observed rhombic EPR signal stayed unclear.

Herein, we have approached the problem of the existing ambiguity related to the EPR spectrum of the $[(TAML)Co^{IV}(O)]^{2-}$–Sc^{3+} motif by re-investigating in detail the electronic structure of the product(s) formed in the reaction of $[(TAML)Co^{III}]^{-}$ and iodosylbenzene (PhIO) in the presence of Lewis or Brønsted acids. Combining advanced spectroscopies, such as X-band EPR, electron nuclear double resonance (ENDOR), XAS/EXAFS, magnetic circular dichroism (MCD), and resonance Raman (rRaman), and theoretical studies, we make an unambiguous assignment of the electronic structures of the two species showing rhombic and isotropic $S = 1/2$ EPR signals, respectively. We demonstrate that, in contrast to our previous $[(TAML)Co^{IV}(O)]^{2-}$–Sc^{3+} assignment, the electronic structures of the products formed are highly multiconfiguration. The oxidation process involves both TAML and cobalt based oxidations, yielding interconvertible $[(Sol)(TAML^{\bullet+})Co^{III}\text{---}OH(LA)]^{-}$ and

[(H-TAML$^{\bullet+}$)Co^{III}=O(LA)]$^{-}$ or a different resonance form [(H-TAML)Co^{IV}=O(LA)]$^{-}$ with distinct spectroscopic and reactivity properties (Scheme 2).[71c] It should be noted that the H of the OH group of **1** comes from H_2O that contains in Li[(TAML)Co^{III}]•3H_2O. The reversible interconversion between Co^{III}---OH and Co^{IV}=O (or Co^{III}=O) forms is dependent on temperature and on LA and involves an intramolecular electron transfer between TAML$^{\bullet+}$ and Co(III), and proton transfer between the hydroxo and TAML ligands together with a concomitant change of the spin-state of Co(III) from $S = 1$ to $S = 0$ (or $S = 1/2$ Co(IV)). Such a LA-assisted interconversion between metal-oxo and -hydroxo forms, which are often proposed to play as key intermediates in the catalytic oxidation of water to give molecular oxygen,[78–82] may emphasize the importance of intramolecular electron and proton movements in chemical and biological oxidation reactions. Our finding of the reversible interconversion between Co^{III}---OH and Co^{IV}=O (or Co^{III}=O) forms, has allowed us to make a rare comparison of the reactivity of the two redox tautomers in oxygen atom transfer (OAT) and hydrogen atom transfer (HAT) reactions.

RESULTS AND DISCUSSION

Addition of PhIO (3 equiv) to an acetone solution of Li[(TAML)Co^{III}]•3H_2O at 253 K did not lead to any reaction, as evidenced by observing no spectral change in the UV-vis absorption spectrum (data not shown). However, the presence of redox-inactive metal ions ($Sc(OTf)_3$ or $Y(OTf)_3$; 2 equiv) or triflic acid (HOTf; 5 equiv) afforded the formation of a blue species **1** with a strong electronic absorption band at 600 nm (ε = 7200 M^{-1} cm^{-1}; Figure 1a, blue spectrum; Supporting Information (SI), Figure S1a).[69,83,84] Interestingly, we observed UV-vis spectral changes of the reaction solution of **1** in the presence of HOTf when the temperature of the reaction solution was lowered from 253 K to 193 K (see the spectral changes from blue spectrum to green spectrum shown in Figure 1a). A decay of the characteristic UV-vis band at 600 nm corresponding to **1** (Figure 1a, blue spectrum) was observed with the concomitant appearance in the absorption features at 353, 700, and 950 nm corresponding to the green species, which is denoted as **2** (Figure 1a, green spectrum); the color of the reaction solution was also changed from blue to green. Interestingly, when the temperature of the reaction solution was increased from 193 K back to 253 K, we observed the complete regeneration of **1** (Figure 1b). These results suggest that the intermediates **1** and **2** are in equilibrium and these species are interconvertible depending on the temperature; **1** is a preferred species at a high temperature (e.g., 253 K), whereas **2** is favored at a low temperature (e.g., 193 K) (see Scheme 2). The interconversion between **1** and **2** was observed over several cycles (Figure 1c), and we observed the presence of both **1** and **2** in the reaction solution at 233 K (SI, Figure S2). Finally, the equilibrium constant K between **1** and **2** has been determined at different temperatures and from the van't Hoff plot, the heat of formation (ΔH) and entropy (ΔS) associated with the conversion of **1** to **2** is experimentally determined to be –8.6 kcal mol^{-1} and –42 cal K^{-1} mol^{-1}, respectively (Figure 2 and SI, Table S1). The K values (LA = HOTf) were found to be proportional to concentration of HOTf in acetone at 233 K (Figure 3 and SI, Table S2), which corroborates an associative mechanism (Scheme S1). Such an associative process may attribute to the experimentally observed negative ΔS value (–42 cal K^{-1} mol^{-1}).

EPR Spectroscopy.

The interconversion between **1** and **2** was also monitored by X-band EPR spectroscopy in solution, which showed no demetallation in the presence of Lewis acids.[85] First, the X-band EPR spectrum of **1** in acetone at 273 K exhibited a broad isotropic signal at $g = 2.2448$ (Figure 4a) (SI, Figure S1b). Upon lowering the solution temperature from 273 K to 193 K, the intensity of the $g = 2.2448$ signal for **1** diminished, and a new signal appeared at $g = 1.9973$ for **2** and became a dominant peak (Figure 4c). Upon rewarming the reaction solution from 193 K to 273 K, the EPR signal at $g = 1.9973$ for **2** disappeared with the reappearance of the $g = 2.2448$ signal for **1** with a full intensity as shown in Figure 4a. These results support the occurrence of the interconversion between **1** and **2**, as demonstrated in the UV-vis experiments. Also, as observed in the UV-vis spectrum (SI, Figure S2), the presence of both **1** and **2** at 233 K was confirmed by taking the EPR spectrum of the reaction solution (Figure 4b). Thus, based on the UV-vis and EPR data, we conclude that there are two interconvertible Co intermediates that are in equilibrium and that the conversion from **1** to **2** requires the association with HOTf (LA) as shown in Scheme S1. Accordingly, the ratio of **1** vs **2** is found to be dependent on the reaction temperatures, as well as on the acid-strength of LA.

Complexes **1** and **2** could also be isolated in pure form as frozen solutions, and EPR measurements at 5K provided further insights into their electronic structures. The EPR spectrum of a frozen acetone solution of the green species **2**, showed a nearly isotropic signal at $g_z = 2.0090$, $g_x = 1.9998$, and $g_y = 1.9840$ with well-resolved ^{59}Co hyperfine splittings of $A_z = 3$ MHz, $A_x = 76$ MHz, and $A_y = 8.4$ MHz (Figure 5a; SI, Figure S3). Notably, the average value ($A_{Co} = 29$ MHz) of the A_z, A_x, and A_y values obtained for **2** in frozen solution agrees with the A value of **2** in solution ($A_{Co} = 28$ MHz) at 193 K within an experimental error (under similar conditions in the presence of HOTf in acetone). This indicates that the sign of the A_z, A_x, and A_y values of **2** is all positive and the EPR spectra obtained in solution (Figure 4c) and frozen (Figure 5a) states correspond to identical species **2**. It should be noted, however, that the ^{59}Co hyperfine splitting values of **2** in the presence of HOTf ($A_z = 3$ MHz, $A_x = 76$ MHz, and $A_y = 8$ MHz) are similar but clearly different from those of **2** prepared in the presence of $Sc(OTf)_3$ (**2**-Sc^{3+}; $A_z = 6$ MHz, $A_x = 87$ MHz, and $A_y = 16$ MHz) (SI, Figure S3). The ^{59}Co hyperfine splitting values of **2** prepared in the presence of $Y(OTf)_3$ (**2**-Y^{3+}; $A_z = 3$ MHz, $A_x = 101$ MHz, and $A_y = 14$ MHz) are also different from those of **2** prepared in the presence of HOTf or $Sc(OTf)_3$ (SI, Figure S3). Such a difference in the ^{59}Co hyperfine splitting values of **2** depending on Lewis and Brønsted acids indicates that Lewis and Brønsted acids interact with the terminal oxo group of **2** (vide infra). Finally, upon rewarming the frozen solution to 193 K, the $g = 1.9973$ signal as shown in Figure 4c was obtained with a full intensity, further confirming that the species isolated in frozen and solution states represent identical species and no decay of **2** occurs during the freeze/thaw process.

The EPR spectrum of a frozen TFE/acetone ($v/v = 19:1$) solution of the blue species **1** (generated in the presence of $Y(OTf)_3$) reveals a rhombic signal with $g_z = 2.6011$, $g_x = 2.1095$, and $g_y = 2.0268$ and a well resolved ^{59}Co hyperfine splitting of $A_z = 3$ MHz, $A_x = 65$ MHz, and $A_y = 3$ MHz (Figure 5b), which is clearly distinct from **2**. It should be noted

that the average value of the A_z, A_x, and A_y values (A_{Co} = 24 MHz) of **2** under frozen conditions at 5K again agrees with the A value obtained in solution at 273 K (A_{Co} = 24 MHz) (Figure 4a), thereby confirming that the electronic structure of **1** remains unaltered in solution and frozen states. This further indicates that the sign of the A_z, A_x, and A_y values of **1**, similar to the case of **2**, is also all positive. Please note that complex **1** could be isolated in pure form in frozen state only in the presence of $Y(OTf)_3$ and TFE. As shown in Scheme S1 the conversion of **1** to **2** is initiated by the association of the Lewis (LA)- or Bronsted(BA)-acids, followed by the concomitant electron- and proton-transfer processes (Scheme S1). Thus, in addition to temperature, the relative concentration of **1** and **2** in the reaction is also dependent on the acid strength of LA/BA. In presence of a strong acid like HOTf both **1** and **2** could be observed in equilibrium in an acetone solution in the temperature range 193 – 273 K (Figure 1, Figure 4). In the case of a weaker acid like $Sc(OTf)_3$ or $Y(OTf)_3$ in acetone, the conversion of **1** to **2** was observed only in a frozen media at 77 K. Further reduction of the acid strength by employing $Y(OTf)_3$ in a protic solvent like TFE ensured that the conversion of **1** to **2** did not occur even at 77 K, which allowed us to obtain a frozen sample of **1** in pure form. The Lewis acidity of $Y(OTf)_3$ with TFE is, however, strong enough to produce **1** by the reaction of $Li[(TAML)Co^{III}]\bullet 3H_2O$ with PhIO. Complex **2** was isolated in pure form in frozen state in the presence of other strong Lewis acids such as $Sc(OTf)_3$, $Y(OTf)_3$, and HOTf in acetone.

In addition, upon rewarming the frozen solution to 253 K, the g = 2.2248 signal, as shown in Figure 4a, was obtained with a full intensity (SI, Figure S4). It is noted that similar ^{59}Co hyperfine splitting values (A_{Co} = 15 – 38 MHz) were reported for the resonance electronic structures of $[(TPP)Co^{IV}(R)(L)]^+$ and $[(TPP^{\bullet+})Co^{III}(R)(L)]^+$ (L = sixth axial base ligand, TPP = tetraphenylporphyrin dianion, and R = alkyl and phenyl groups) complexes depending on the basicity of L.[86] A slightly larger ^{59}Co hyperfine splitting value (A_{Co} = 42 MHz) was reported for $[(DH)_2Co^{IV}(R)(L)]^+$ (DH^- = dimethylglyoxime anion).[87–89] The spin quantification based on the signals of **1** and **2** at 233 K accounts for the coexistence of both species in solution with a total of 100% yield (SI, Figure S5). This corroborates the quantitative conversion of $Li[(TAML)Co^{III}]\bullet 3H_2O$ to **1** or **2** by PhIO in the presence of Lewis or Brønsted acids.

CSI-MS Spectrometry.

The cold-spray ionization time-of-flight mass spectrometry (CSI-MS) measurements were performed for **2**, which was generated in the presence of $Sc(OTf)_3$ in acetone, exhibiting two prominent ion peaks at a mass-to-charge (m/z) ratio of 785.1010 and 803.1042 in negative mode corresponding to in situ generated cobalt(III) complexes such as $[(TAML)Co(^{16}O)(Sc)(CH_3CN)_2(CH_3OH)_2(CF_3SO_3)]^-$ (calcd. m/z = 785.1057) and $[(TAML)Co(^{16}O)(Sc)(CH_3CN)_4(CF_3SO_3)]^-$ (calcd. m/z = 803.1064), respectively, as reported previously.[69] CH_3CN and CH_3OH detected in the CSI-MS spectra came from solvents which were used to dissolve PhIO and $Sc(OTf)_3$.[69]

These two peaks shifted by two-mass unit when $PhI^{18}O$ was employed in the synthesis of **2**, thereby confirming that **2** contains one oxygen atom derived from PhIO.[69] Complex **1** also contains an oxygen atom derived from PhIO. A prominent mass peak at m/z =

446.1 corresponding to $[(TAML)Co(^{16}O)(H)]^+$ (calcd. m/z = 446.3) was observed in positive mode for **1** (SI, Figure S6), which was generated in acetone at 233 K in the presence of HOTf, which shifted by two-mass unit when $PhI^{18}O$ was used in the synthesis (SI, Figure S6, inset). Notably, $[(TAML)Co(^{16}O)(H)]^+$ may represent the two-electron oxidized form of $[(TAML)Co(^{16}O)(H)]^-$, which is not unusual considering the non-innocent behavior of the $TAML^{4-}$ ligand. We would like to stress again that the observed signals represent the stability of a particular ion under the CSI-MS conditions and may not represent the bulk species present in solution. The deprotonation, oxidation and the reduction processes observed under the CSI-MS conditions are not uncommon in the literature.[90] So, the reported mass data cannot be used to judge the purity of the sample or to assign the oxidation state of metals in the sample in bulk solution. However, it unambiguously demonstrates the presence of one oxygen atom in both **1** and **2**.

XAS Spectroscopy.

Complexes **1** and **2** were subjected to cobalt K-edge X-ray absorption spectroscopy under frozen conditions at 4 K (see experimental section for sample preparation; **1** is prepared by employing $Y(OTf)_3$ in TFE, and **2** by employing $Sc(OTf)_3$ or $Y(OTf)_3$ in pure acetone). The Co K-edge X-ray absorption near edge spectroscopy (XANES) of $[(TAML)Co^{III}]^-$, **1**, and **2** in the presence of $Sc(OTf)_3$ and $Y(OTf)_3$ are shown in Figure 6. It is noted that there is an ~1.3 eV blue shift in the edge of **1** and **2** vs $[(TAML)Co^{III}]^-$, indicative of significant Co(IV) character. The XANES of $[(TAML)Co^{III}]^-$ and **1** are both indicative of cobalt contained in a centrosymmetric coordination geometry; each contains a weak pre-edge feature at 7710.6(4) eV corresponding to the quadrupole allowed dipole forbidden Co(1s → 3d) transition, and a higher energy ill resolved shoulder at 7715.3(2) eV ($[(TAML)Co^{III}]^-$) and 7717.2(2) eV (**1**) corresponding to the nominal dipole allowed Co(1s → 4p) + LMCT transition. In contrast, **2** in the presence of both $Sc(OTf)_3$ and $Y(OTf)_3$ displays an intense pre-edge feature at 7711.3(1) eV. As the intensity of the pre-edge feature of **2** is too great to arise from electric-quadrupole transitions, its intensity likely derives through Co 3d-4p mixing allowed by low symmetry distortions.[91,92] Since electric-dipole transitions are substantially more intense than electric-quadrupole transitions, only a small amount of 3d-4p mixing is required to cause a sizable increase in pre-edge peak intensity. Further, the intensity of the pre-edge feature is similar to that found previously in Co-oxo complexes,[65–69] suggestive of a short axial ligand. Analysis of the EXAFS data was consistent with this formulation.

The EXAFS region for **1** was best modeled as a 6-coordinate Co-center with 4 Co-N scatters at 1.82 Å corresponding to the equatorial TAML ligand, and 2 Co-O scatters at 2.3 Å corresponding to weakly associated OH^-/acetone ligands (SI, Table S3). It should be noted that satisfactory solutions to the EXAFS data for **1** could also be located for a 4-coordinate species, and thus the square-planar coordination geometry of **1** cannot be ruled out based on the XAS data alone.

In the presence of $Y(OTf)_3$, we best model **2** as a 5-coordinate species[93] with 4 Co-N scatters at 1.84 Å and a short Co-O scatterer at 1.68 Å. In addition, a long, well-ordered Co•••Y vector could be located at 3.98 Å (SI, Table S4). Thus, we formulate **2** in the presence of $Y(OTf)_3$ as a Co-O species with a Y^{3+} cation coordinated with the Co-O moiety.

Replacement of $Y(OTf)_3$ with $Sc(OTf)_3$ resulted in a similar structure; we find 4 Co-N scatters at 1.82 Å, 1 Co-O scatterer at 1.72 Å, and a Co•••Sc vector at 3.12 Å (SI, Table S5). The increase in the Co-O bond length upon replacement of Y^{3+} with Sc^{3+} is consistent with the observed pre-edge features; we find that the integrated area of the pre-edge transition of **2** in the presence of Y^{3+} is 11% greater than that in the presence of Sc^{3+}. This increase in intensity is related to an increase in 4p character to the acceptor state, which would be expected for a contraction of the Co-O bond length, which is reflected in the contraction of the Co-O bond length by 0.04 Å.

Pulse EPR Spectroscopy.

Further evidence for the presence of a terminal Co=O unit in **2** but not in **1** comes from multi-technique pulse EPR spectroscopic measurements (Figure 7; SI, Figure S7). The 34 GHz Davies ^{17}O ENDOR spectra of **2**, generated in the presence of $PhI^{17}O$ and $Sc(OTf)_3$ in acetone, exhibit two ENDOR frequencies centered at the Larmor frequency of ^{17}O ($\nu_N \approx 7$ MHz) as shown in Figure 7a, which are absent in the corresponding spectra of the complex generated in presence of $PhI^{16}O$ (SI, Figure S8; black line), thereby confirming their origin from the coupling of the ^{17}O nucleus to the cobalt ion. A hyperfine tensor $A = [4.7, 7.1, 7.1]$ MHz was determined from the separation of the two peaks, which is comparable with the reported hyperfine values of 4 – 7 MHz for the oxygen atom of metal-oxo complexes.[94–96] The determined isotropic hyperfine coupling constant, $|A_{iso}(^{17}O)| \approx 6.3$ MHz, corresponds to a spin-density of only 5% at the ^{17}O nucleus, which is much less than expected for an oxyl radical.[97] Notably, no signals were detected in the ENDOR spectra of the ^{17}O-labeled **1**, which is in full consistence with the XAS data that reveal a much longer Co-O(H) separation in **1**, as compared to that in **2**.

Along with the ^{17}O ENDOR, we have successfully detected the ^{17}O signal using 9 GHz HYSCORE. The HYSCORE spectrum taken at 348.4 mT is displayed in Figure 6b. The (–,+) quadrant shows a cross-peak at (–1.3, 5.3) MHz, which was not observed in the spectrum of the complex prepared by presence $PhI^{16}O$ (SI, Figure S9). These results strongly suggest that the cross-peak arises from the ^{17}O nucleus coupled to the cobalt ion. The cross-peak is split by approximately twice the Larmor frequency of ^{17}O and is centered at ~A/2, which gives an estimate of the hyperfine coupling of ^{17}O. The resulting simulation data using the Hamiltonian parameters obtained from the ^{17}O Davies ENDOR nicely match the experimental data (Figure 7b). The quadrupole tensor should be small;[97] otherwise, the line shape of the cross-peak cannot be reproduced in the simulation.[98]

Magnetic Circular Dichroism Spectroscopy.

MCD measurements provided further insights into the electronic structures of **1** and **2**. Prior to oxidation, the purple square planar $[(TAML)Co^{III}]^-$ complex displays a major electronic absorption band at 19700 cm^{-1}, which is accompanied by the intense derivative-shaped MCD features (Figure 8, purple trace; SI, Figure S10). These indicate that at least two different electronic transitions contribute to the major absorption band, exhibiting the maximum intensities at 40 K and diminishing at lower temperatures (SI, Figure S11a). This magnetization behavior was fitted with an $S = 1$ Co(III) center with a positive zero-field splitting (D) of ~48 cm^{-1} (SI, Figure S11b),[99] which is comparable to the value previously

obtained for other square-planar $S = 1$ Co(III) complexes.[100] The pseudo-A term MCD feature indicative of the presence of near-degenerate Co d_{xz}- and d_{yz}- based SOMOs is also observed in **1**, which suggests that the Co(III) oxidation state and $S_{Co} = 1$ spin state are retained in **1**. However, compared to $[(TAML)Co^{III}]^{-}$, **1** displays additional absorption and MCD features at energies below 16000 cm^{-1} (Figure 8, blue trace; SI, Figure S12). These features are associated with new ligand-based transitions, where the acceptor MO is a TAML-based hole generated upon oxidation of $[(TAML)Co^{III}]^{-}$ to form $[(TAML^{+\bullet})Co^{III}]^{-}$, supporting the redox non-innocence of the TAML ligand (Figure S13). Complex **2** displays near-IR absorption and MCD features similar to **1**, although it lacks the pseudo-A MCD feature in the visible region (Figure 8, green trace; SI, Figure S14). This presumably indicates a change in spin state from S_{Co}=1 in **1** to S_{Co}=0 for the Co(III) state in **2**, which is also supported by theoretical studies (SI, Figure S13).

Resonance Raman Spectroscopy.

rRaman spectra of **1** and **2** did not show any $^{16/18}O$-isotope sensitive bands that could be assigned to the Co=O vibrations. However, compared to the rRaman spectrum of $[(TAML)Co^{III}]^{-}$ (Figure 9a, violet trace), those of **1** (Figure 9a, blue trace) and **2** (Figure 8a, green trace) display new features at ~1100 and ~1700 cm^{-1}, ascribed to the vibrations associated with the amidate moiety of the oxidized TAML ligand (Figure 9c; see Theoretical Studies below), that are significantly shifted from that of $[(TAML)Co^{III}]^{-}$ (Figure 9a, violet trace). Moreover, **2** exhibits two new low-energy rRaman features at 620 and 698 cm^{-1}. These signals are sensitive to deuterated perturbation and gain in intensity because of the distortions associated with the protonation on amido nitrogen of the TAML ligand (SI, Figure S15).

Theoretical Studies.

The spectroscopic observations described above reveal that despite their equal composition, **1** and **2** exhibit significant differences in their electronic and geometric structures. Based on theoretical studies we propose that structurally, the two complexes differ in their protonation site.[101] While **1** is protonated at the oxo ligand, thereby creating a hydroxo moiety, **2** is most likely protonated at one of its amido groups of the TAML ligand (see Scheme 2 and SI, Figure S16).[102] In agreement with the above results from EXAFS, our geometry optimizations at the DFT level of theory predict an increase of the average Co–N distance by 0.08 Å upon such a proton shift (see SI, Table S6). Moreover, the predicted Co–O distance decreases from 2.11 Å in **1** to 1.85 Å in **2**, thus showing the same trend as the EXAFS fitted Co-O distances. The Co–O bond distance in **1** is found to be slightly elongated by 0.02 Å when a solvent molecule acetone weakly binds to the Co-moiety (see discussion below). It should be noted that while the trend of the EXAFS estimated Co-O bond lengths is correctly reproduced, the absolute values deviate notably (SI, Table S6). This discrepancy is frequently encountered in metal-oxo chemistry.[103–105] Nevertheless, the potential energy surface (PES) of these complexes along the Co–O bond vector is nearly flat, and the energy required for fitting the EXAFS-determined Co–O bond lengths lies within ~2 kcal mol^{-1} for both complexes (SI, Figure S17). Such a finding is entirely consistent with the above findings that different Lewis acids have a large impact on the axial Co-O bond of **2**.

We have proposed above the aliphatic amido-site as the most likely proton acceptor for the following reasons. The rapid interconversion between **1** and **2** would necessitate a readily available proton source that would not be provided by acetone, which is an aprotic solvent. Thus, ligand protonation seems most likely. Paramagnetic resonance studies rule out the short oxo-ligand of **2** as being protonated. Of the remaining basic sites found in **2**, the TAML aliphatic amido nitrogen is the most basic – protonation of that nitrogen is ~19.5 kcal/mol more stable than protonation of other basic sites (SI, Table S7).

Although the PES for the axial Co-O bond of **1** and **2** is nearly flat, the character and geometric arrangement of the axial ligand have a critical influence on the electronic structure of the Co center. A square pyramidal ligand field, as imposed by the TAML and hydroxo ligands, splits the Co d-orbitals according to (d_{xy}), (d_{xz}, d_{yz}), (d_z^2), and (d_x^2-$_y^2$), as illustrated in Figure 10. Clearly, the energetic order of the orbital groups and hence potential ground state configurations are determined by the relative strength of the axial and equatorial ligand field. Furthermore, the TAML frontier **π** and **π*** orbitals allow for an easy charge transfer between the metal and the ligand, thereby giving **1** and **2** access to an additional set of low-lying electronic configurations. Hence, various electronic configurations with the Co center in different oxidation states could potentially contribute to the electronic ground states of **1** and **2**. This assessment is in line with the findings of Meeus et al.,[106] who found the ground state of a structurally related Co complex to also be of highly multiconfigurational character.

Figure 10 depicts a set of configurations that we found to be important in fully describing the electronic structures of **1** and **2**. Moreover, Table 1 lists the most important contributions from these configurations to the electronic ground states of **1** and **2** (SI, Tables S8 – S10). According to our NEVPT2 (13,9) calculations for **1** with a constrained Co–OH bond length of 2.40 Å, the electronic ground state is dominated by configuration **C** that corresponds to a Co(III) center with a local spin of S_{Co} = 1 that is antiferromagnetically coupled to the S_L = 1/2 spin of a ligand-based radical. While this ground state composition nicely explains the observed MCD spectrum (see Figure 8) on account of the two holes in the (d_{xz}, d_{yz}) shell, it does not infer the measured *g*-tensor. While 'in-state' spin-orbit coupling (SOC) through the $\hat{l}_z$ operator is impossible owing to the occupation pattern, coupling through the $\hat{l}_x$ or $\hat{l}_y$ components of the SOC operator to other, excited configurations is effectively diminished by large energy separations according to our results. Therefore, an isotropic *g*-tensor (g_{iso} = 2.00) is predicted which contradicts the experimental observation. Strong SOC leading to a rhombic *g*-tensor with one large *g*-value may arise from configurations with only a single hole in a near-degenerate (d_{xy}, d_{yz}) orbital shell, as presented in configuration **B**.[107] The importance of configuration **B** relative to configuration **C** is expected to grow with increasing axial ligand field strength, since this infers destabilization of the d_z^2-orbital relative to the (d_{xz}, d_{yz}) orbital shell. Following this argument, a solvent molecule has been added to the computational model in an axial position. Such an addition is well in line with the diminished Co K pre-edge intensity of **1**, which is demonstrated by the calculated spectra shown in SI, Figure S18. On account of the weak **σ**-donor character of the solvent, the Co–O bond distance is predicted to be rather long (3.0 – 3.2 Å depending on the Co–OH bond distance), indicating a weak bonding. However, the altered ligand

field induces a significant shift of the ground state composition. With a fixed Co–OH bond distance of 2.50 Å, the electronic ground state features significant contributions from configurations **B** (29%) and **C** (20%) as well as configuration **A** (28%) that has Co(II) character. Importantly, two low-lying excited states are predicted at 1844 and 3150 cm^{-1}, respectively, giving rise to strong SOC effects, which in turn leads to a rhombic *g*-tensor with *g* values of 1.91, 2.32, and 2.99. Furthermore, owing to the considerable contributions from configuration **C** with two holes in (d_{xz}, d_{yz}) orbital shell, this ground state composition also agrees well with the observed MCD spectrum of **1**. At this point, it should be noted that the ground state composition and hence the calculated *g*-values vary with the Co–O bond distance (see Supporting Information). Notwithstanding the inherent methodological error sources and the concomitant numerical uncertainties concerning the actual values of Co–O bond lengths, our results clearly demonstrate that only a multiconfigurational ground state with significant contributions from configurations **B** and **C** is able to conclusively explain all spectroscopic observations. Moreover, the delicate connection between the axial field strength and the ground state composition renders the inclusion of a weakly bound sixth ligand in **1** necessary.

For the electronic ground state of **2**, Co(III)L• configuration **D** is important. Owing to its lack of low-lying excited states and hence any strong SOC effects, the calculated *g*-tensor shows little rhombicity and a g_{iso} value of 2.08. This demonstrates that the protonation site dramatically influences the local electronic structure at the metal center. In addition, considerable contributions from configuration **E** with Co(IV) character are predicted.

Time-dependent density functional theoretical (TDDFT) calculations could also reproduce the experimental trends in MCD. For $Li[(TAML)Co^{III}]•3H_2O$, the major absorption band can be assigned to charge transfer (CT) transitions from TAML to the near-degenerate $(d_{xz})^1(d_{yz})^1$ orbitals, which are strongly spin-orbit coupled to exhibit the pseudo-A term MCD feature (SI, Table S11 and Figure S10). This pseudo-A term feature is retained in the spectra of **1** because of the presence of spin-orbit coupled near degenerate $(d_{xz})^2(d_{yz})^1(d_z{}^2)^1(L_{\pi*})^1$ and $(d_{xz})^1(d_{yz})^2(d_z{}^2)^1(_{L\pi*})^1$ states, as also evidenced from the large g_3 tensor in the X-band EPR spectrum (SI, Table S12 and Figure S12). The orbital degeneracy is, however, lifted in **2,** containing a low-spin Co(III) center, which explains the lack of any pseudo-A term feature in the spectrum of **2** (SI, Table S13 and Figure S14). The additional low energy features observed in **1** and **2** are intra-ligand charge transfer transitions associated with a TAML-based SOMO.

The redox-active HOMO of $[TAML)Co^{III}]^-$ is C=O **π***-antibonding and C-N **π**-bonding in character (Figure 9b), which explains the experimental trends in the rRaman spectra. Upon oxidation, the C=O and C-N stretching vibrations of the carboxamide groups adjacent to the phenyl ring can shift up by 58 cm^{-1} and down by 246 cm^{-1}, respectively, in **1** and **2**, which explain the presence of the additional bands at 1100 and 1700 cm^{-1} (Figure 9). Complex **2** exhibits additional new low energy rRaman features, which, as shown in SI, Figure S15, gain intensity because of the distortions associated with the protonation of the TAML ligand.

Reactivity Studies of 1 versus 2.

The reactivity of **1** at 298 K was reported previously.[69] In this study, we compared the reactivities of **1** and **2** in oxygen atom transfer (OAT) and hydrogen atom transfer (HAT) reactions under the identical conditions (see Experimentation Section for reaction conditions). First, the OAT reactions by **1** and **2** were investigated. When thioanisole was added to the reaction solutions of **1** and **2** at 233 K, both **1** and **2** disappeared with the time traces showing the first-order kinetics profiles. We also found that the rate constants increased linearly with the increase of the thioanisole concentration, affording the second-order rates of 2.2 M^{-1} s^{-1} for **1** and 9.7 × 10^{-2} M^{-1} s^{-1} for **2** (SI, Figures S19b and 20b). The latter results demonstrate that the reactivity of **1** is ~23 times greater than that of **2** in OAT reactions. The second-order rate constants (k_2) for the OAT reactions of **1** and **2** with *para*-X-substituted thioanisoles, *p*-X-$C_6H_4SCH_3$ (X = OMe, Me, H, F, and Cl) were also determined in acetone at 233 K (SI, Table S14 and Figures S19 and S20). Since the first-order rate constants of **1** and **2** were proportional to concentrations of *para*-X-substituted thioanisoles, interconversion between **1** and **2** was much slower than OAT reactions in determination of the k_2 values. The electrophilic nature of **1** and **2** in OAT reactions were determined by Hammett plot of the second-order rate constants against Hammett parameter (σ_p) of *para*-X-substituents, affording the ρ values of –2.4 for **1** and –7.6 for **2** (Figure 11).[108,109] The ρ value of –2.4 for **1** agrees well with that reported for **1** obtained by the reaction of $[(TAML)Co^{III}]^-$ with PhIO in the presence of $Sc(OTf)_3$ instead of HOTf in acetone.[69] The larger ρ value for **2** as compared with **1** is consistent with the expected higher electrophilicity of a $Co^{III/IV}$=O moiety in **2** as compared to a Co^{III}-OH moiety in **1**. Plots of log k_2 vs the one-electron oxidation potentials (E_{ox}) of *para*-substituted thioanisoles are shown in Figure S21 (SI, Table S14), where **2** affords a large slope of –9.1, in contrast, **1** affords a smaller slope (– 4.9). The negative slopes indicate that the reactions are electrophilic; however, it should be noted that the larger slope does not necessarily mean more electrophilic (or more contribution of electron transfer) because of different compensation effects of activation entropies depending on oxidants and temperature.[90]

The more entropy-controlled OAT reactivity of **1** as compared with **2** is shown in the Eyring plot of the k_2 values of OAT from **1** (blue line) and **2** (green line) to thioanisole in Figure 12 and Table S15, where the $\Delta S^{\ddagger}$ value for **1** ($\Delta S^{\ddagger}$ = –32 cal K^{-1} mol^{-1}) is significantly less negative than **2** ($\Delta S^{\ddagger}$ = –41 cal K^{-1} mol^{-1}). On the other hand, the activation enthalpy for **1** ($\Delta H^{\ddagger}$ = 5.6 kcal mol^{-1}) is larger than **2** (5.0 kcal mol^{-1}) of OAT. Such difference in the $\Delta H^{\ddagger}$ and $\Delta S^{\ddagger}$ values between **1** and **2** may result from the difference in the electronic configurations between **1** and **2** (vide supra). Whereas **1** is predominantly $[(TAML^{\bullet+})Co^{III}\text{-}OH]^-$ with a non-innocent TAML ligand, complex **2** has significant $[(TAML\text{-}H)Co^{IV}=O]^-$ character (Scheme 2 and Figure 10). Thus, the O-atom transfer reaction by **1** requires the electron-transfer reduction of the $TAML^{\bullet+}$ ligand, the concomitant S–O bond formation and deprotonation of the O–H bond. The $\Delta S^{\ddagger}$ value is therefore less negative (–32 cal K^{-1} mol^{-1}) in OAT mediated by **1**, because of the higher contribution of the electron transfer pathway.[90] In contrast, a concerted OAT from the $[(TAML\text{-}H)Co^{IV}=O]^-$ moiety of **2** may have more geometrically restricted transition state to afford the more negative $\Delta S^{\ddagger}$ (–41 cal K^{-1} mol^{-1}) and smaller $\Delta H^{\ddagger}$ value (5.0 kcal mol^{-1}).

The product analysis by ESI-MS and EPR spectroscopy of the reaction solutions of **1** and **2** with thioanisole showed the formation of $[Co^{III}(TAML)]^-$ (SI, Figures S22 and S23). GC and GC-MS data of the oxidation of thioanisole by **1** and **2** revealed the formation of methyl phenyl sulfoxide. In addition, the ^{18}O-labeling experiments performed with **1**-^{18}O and **2**-^{18}O revealed that the oxygen atom in the methyl phenyl sulfoxide contained 33(3)% and 55(3)% ^{18}O, respectively (SI, Table S16 and Figures S22 and S23). As mentioned in the Experimental Section, labelled $H_2{}^{18}O$ is used to prepare $PhI^{18}O$. It is not possible to exchange 100 % of PhIO to $PhI^{18}O$. Thus, due to residual PhIO, ^{16}O-labelled **1** or **2** is generated, reacting with thioanisole to produce ^{16}O-labelled methyl phenyl sulfoxide product. It is noted that the degree of the ^{18}O-incorporation into **1** or **2** depends on the relative rates of the ^{18}O-exchange between PhIO and $H_2{}^{18}O$. Thus, the higher ^{18}O incorporation for **2** as compared with that for **1** may result from the faster ^{18}O exchange of **2** with $H_2{}^{18}O$ or the slow reaction between **2** and thioanisole. In the latter case, **2** has more time to exchange with $H_2{}^{18}O$ to form ^{18}O-labeled **2**, giving a high ^{18}O-incorporation into the methyl phenyl sulfoxide product.

We also investigated HAT reactions by **1** and **2**. The rate constants of HAT from 1,4-cyclohexadiene to **1** and **2** were determined at 233 K (SI, Figure S24). The decay profiles of **1** (SI, Figure S24a) and **2** (SI, Figure S24c) showed the first-order kinetics. The second-order rate constant of HAT of **1** in acetone at 233 K (SI, Figure S24b) is 44 times larger than that of **2** under the same reaction conditions (SI, Figure S24d).[36] HAT reactions of **1** and **2** were also compared using 2,6-di-*tert*-butyl phenol (2,6-DTBP) as a hydrogen donor (SI, Figure S25 and Figure S26). The second-order rate constants (k_{ox}) were determined and listed in Table S17. Eyring plots ($\log(k_2/T)$ vs T^{-1}) of HAT reactions from 2,6-DTBP to **1** and **2** are shown in Figure 13, where the intercepts and slopes afforded the activation enthalpies ($\Delta H^{\ddagger}$ = 8.0 kcal mol^{-1} for **1** and 5.0 kcal mol^{-1} for **2**) and the activation entropy ($\Delta S^{\ddagger}$ = –21 cal K^{-1} mol^{-1} for **1** and –39 cal K^{-1} mol^{-1} for **2**). The smaller $\Delta H^{\ddagger}$ value for **2** may result from the more favorable proton transfer pathway from 2,6-DTBP to the oxo moiety of **2** than that to the hydroxo moiety of **1**, coupled with the subsequent electron transfer step. The smaller $\Delta H^{\ddagger}$ value for **2** is compensated by the more negative $\Delta S^{\ddagger}$ value for **2**.

In contrast, the proton-transfer pathway from 2,6-DTBP to the oxo moiety of **2**, coupled with electron transfer to the Co(IV) moiety, requires more geometrical restriction as compared with electron transfer, resulting in the more negative $\Delta S^{\ddagger}$ value for **2**. Notably, the difference in the activation entropies due to the difference in the electronic configurations between **1** and **2** is more pronounced for HAT reactions ($\Delta S^{\ddagger}$ = –21 cal K^{-1} mol^{-1} for **1** and –39 cal K^{-1} mol^{-1} for **2**) than in OAT ($\Delta S^{\ddagger}$ = –32 cal K^{-1} mol^{-1} for **1** and –41 cal K^{-1} mol^{-1} for **2**).

In HAT reactions conducted by **1** and **2**, the inorganic product was characterized using ESI-MS and EPR, revealing it to be Co(III) (SI, Figures S27-30). Simultaneously, the organic product was identified through GC analysis (SI, Table S16).

CONCLUSION

In a previous study we reported the formation of a highly reactive low-spin (S = 1/2) Co^{IV}=O intermediate in the reaction of [(TAML)Co^{III}]$^{-}$ with PhIO in the presence of various LAs. The Co^{IV}=O assignment was made based on UV-vis absorption and reactivity studies in solution phase and spectroscopic characterizations (EPR and XAS) under frozen conditions. Based on the present study, we now show that the species characterized in solution and in frozen states are different. That is, we have identified two temperature dependent interconvertible cobalt-oxygen TAML intermediates; a blue species [(Sol)(TAML$^{\bullet+}$)Co^{III}---OH(LA)]$^{-}$ (**1**) where the oxo moiety is protonated to form a hydroxide complex at higher temperatures (e.g., 253 K) and is converted to a green species (**2**) at low temperatures (e.g., in frozen media), as shown in Scheme 2. The assignment of the blue species **1** was made based on XAS, MCD, EPR and ENDOR techniques. For the green species **2**, EXAFS, MCD, pulsed EPR, and ENDOR measurements support the multiconfiguration character of the electronic structure with contributions of the [(H-TAML$^{\bullet+}$)Co^{III}=O(LA)]$^{-}$ state, where a low-spin S = 0 Co^{III} center is bound to a one-electron oxidized TAML ligand, which is protonated and also the [(H-TAML)Co^{IV}=O(LA)]$^{-}$ state. The Co^{IV} character in **2** is well manifested by the large ^{59}Co hyperfine splitting values, which are slightly different depending on Lewis acids, such as HOTf, $Sc(OTf)_3$, and $Y(OTf)_3$. A little oxyl character of **2** has also been clearly indicated by the small ^{17}O hyperfine splitting detected by ENDOR. At elevated temperatures, **2** tautomerizes to [(Sol)(TAML$^{\bullet+}$)Co^{III}---OH(LA)]$^{-}$ (**1**), whereby H^{+} moves from the H-TAML backbone to the oxo moiety with the concomitant change in the spin-state of Co(III) to S = 1. While the Co(IV) state (**E** in Figure 11) contributes to the electronic structures of both **1** and **2**, its contribution is significantly higher for the latter complex with a short Co=O distance. Complexes **1** and **2** can also be generated by employing other Lewis and Brønsted acids. A temperature-dependent reversible interconversion in solution has been identified in the presence of Brønsted acid in the temperature range of 193 K to 253 K. Not only the reactivity at a fixed temperature but also the activation parameters ($\Delta H^{\ddagger}$ and $\Delta S^{\ddagger}$) of **1** and **2** for OAT and HAT reactions were determined to demonstrate how different electronic configurations between **1** and **2** affect the reactivity and the activation parameters. Thus, the present study provides valuable insights into the structure and reactivity of Co−O complexes with different electronic configurations. In particular, our findings provide detailed insights into secondary coordination sphere interactions that can not only tune the equilibrium between the metal-oxo and -hydroxo cores of late-transition metal complexes but also the reactivities in oxygen atom transfer and hydrogen atom transfer reactions depending on temperature.

EXPERIMENTAL SECTION

Materials.

All chemicals were purchased from Sigma-Aldrich Chemical Co., Alfa, and TCI. Chemicals are used as received unless otherwise noted. Solvents were distilled according to reported procedures under an Ar atmosphere prior to use.[110] H_4TAML (H_4TAML = 3,4,8,9-tetrahydro-3,3,6,6,9,9-hexamethyl-1H-1,4,8,11-

benzotetraazo-cyclotridecane-2,5,7,10-(6H,11H)-tetrone) was purchased from GreenOx Catalyst Inc. (Pittsburgh, PA).[111] Iodosylbenzene (PhIO) was prepared by following the literature procedure.[112] The starting cobalt(III) complex, Li[Co(TAML)]•3(H_2O) was synthesized by following the literature procedure with readily available starting materials.[69] $H_2{}^{18}O$ (98% ^{18}O-enriched) and $H_2{}^{17}O$ (70% ^{17}O-enriched) were purchased from Cambridge Isotope Inc. (USA).

Instrumentation.

UV-vis spectra were recorded with Hewlett Packard 8453 diode array spectrophotometers equipped with a UNISOKU Scientific Instruments Cryostat USP-203A for low-temperature experiments. Cold spray ionization time-of-flight mass (CSI-MS) spectra were collected on a JMS-T100CS (JEOL) mass spectrometer equipped with the CSI source. Typical measurement conditions are as follows: needle voltage: 2.2 kV, office 1 current: 50–500 nA, office1 voltage: 0 to 20 V, ringlens voltage: 10 V, ion source temperature: 273 K, spray temperature: 233 K. The CSI-TOF mass spectra of **1** and **2** were observed by directly infusing the reaction solution into the ion source through a pre-cooled tube under high N_2 gas pressure. The samples were directly infused into the source at 20 μL/min to collect electrospray ionization mass (ESI MS) spectra on a Thermo Finnigan (San Jose, CA, USA.) LCQTM Advantage M.A.X. quadrupole ion trap instrument. The shower voltage was set at 3.7 kV and the slim temperature at 193 K. X-band CW-EPR spectra were recorded at 5 Kelvin using an X-band Bruker EMX-plus spectrometer equipped with a dual-mode cavity (ER 4116DM). The low temperature was achieved and controlled with an Oxford Instruments ESR900 liquid He quartz cryostat with an Oxford Instruments ITC503 temperature and gas flow controller. The experimental parameters for EPR measurements were as follows: microwave power = 1.0 mW, modulation amplitude = 10 G, gain = 1×10^4, Microwave frequency = 9.647 GHz, and modulation frequency = 100 kHz. JEOL X-band spectrometer (JES-FA100) with microwave power = 1.0 mW, modulation amplitude = 1.0 mT, microwave frequency = 9.028 GHz, time constant = 0.03 s, and modulation frequency = 100 kHz were used to record X-band electron paramagnetic resonance (EPR) spectra at temperatures ranging from 273 K to 193 K.

Generation of Cobalt-Oxygen Species.

The intermediates, $[(Sol)(TAML^{\bullet+})Co^{III}\text{---}OH(LA)]^-$ (**1**) and $[(H\text{-}TAML)Co^{IV}{=}O(LA)]^-$ (**2**) (Sol = solvent, LA = Lewis acid or Brønsted acid) were prepared by reacting Li[$(TAML)Co^{III}$]•3H_2O with PhIO (3.0 equiv), followed by the addition of Lewis acid ($Sc(OTf)_3$ or $Y(OTf)_3$; 2.0 equiv) or Brønsted acid (HOTf ; 5.0 equiv) to a reaction solution in acetone at 253 and 193 K, respectively. **1** for the CSI-MS measurements, which were recorded in positive mode, was prepared by reacting Li[$(TAML)Co^{III}$]•3H_2O with PhIO (3.0 equiv dissolved in MeOH), followed by the addition of HOTf (2.0 equiv) in acetone at 233 K. ^{18}O-labeled **1** was generated by incubating PhIO (3.0 equiv, dissolved in MeOH) in the presence of ^{18}O-labeled water (5.0 μL, $H_2{}^{18}O$) prior to the reaction with Li[$(TAML)Co^{III}$]•3H_2O and HOTf (2.0 equiv). However, it should be noted that the CSI-MS spectrum of **2**-Sc^{3+} previously reported was recorded in negative mode at 233 K.[69] **2**-Sc^{3+} was prepared by reacting Li[$(TAML)Co^{III}$]•3H_2O with PhIO (3.0 equiv dissolved in

MeOH), followed by the addition of $Sc(OTf)_3$ (3.0 equiv) in acetone:CH_3CN (4:1) at 233 K.[69]

Pulse EPR Spectroscopy.

All Pulse EPR measurements were carried out at Korea Basic Science Institute (KBSI) in Seoul, Korea. ^{17}O-labeled **2**-Sc^{3+} was synthesized by incubating PhIO (3.0 equiv) in the presence of ^{17}O-labeled water (5.0 μL, $H_2{}^{17}O$) prior to its reaction with $Li[(TAML)Co^{III}]\cdot 3H_2O$ (2.0 mM) and $Sc(OTf)_3$ (2.0 equiv) in acetone/CH_2Cl_2 (*v/v* = 1:1) at 213 K. EasySpin was used for the simulations of the EPR spectra.[113] 9/34 GHz (X/Q-band) Pulse EPR data were obtained on a Bruker Elexsys E580 spectrometer and Cryogenic temperatures were achieved with an Oxford CF-935 cryostat and Oxford ITC temperature controller. 9 GHz (X-band) pulse EPR data were acquired using a Bruker EPR 4118X-MD5 dielectric ring resonator. The measurements were conducted at 5 K. The X-band HYSCORE experiments were carried out using a four-pulse sequence, $\pi/2$-τ-$\pi/2$-t_1-π-t_2-$\pi/2$-τ-echo, with pulse length $t_{\pi/2}$ = 16 ns and t_π = 32 ns. The τ value was fixed but t_1 and t_2 were varied with a step size of 16, 32 ns. 34 GHz (Q-band) pulse EPR data were collected using an EN5107D2 resonator. The measurements were conducted at 20 K. The ^{17}O Davies ENDOR were performed using the π-T-$\pi/2$-τ-π-echo, with microwave pulse lengths of $t_{\pi/2}$ = 50 ns, t_π = 100 ns and an inter-pulse time of τ = 300 ns. In this sequence, the RF power is applied during the time T (40 μs) to drive nuclear spin transitions. The repetition time was 6 ms. CW W-band (94 GHz) EPR data were obtained on a Bruker Elexsys E680 spectrometer with a cylindrical high Q-resonator (EN680–1021H) and cryogenic temperatures were achieved with an Oxford CF-935 cryostat and Oxford MercuryiTC temperature controller. The spectrum was obtained with the following experimental parameters: microwave frequency, 93.954 GHz; microwave power, 0.5 μW; modulation amplitude, 10 G; time constant, 81.92 ms; 16 scans. The measurements were conducted at 80 K.

Absorption and MCD Spectroscopies.

A homogenous sample of intermediate **1** was prepared by reacting $Li[(TAML)Co^{III}]\cdot 3H_2O$ (2.0 mM) with PhIO (3.0 equiv) in the presence of $Y(OTf)_3$ (2.0 equiv) in TFE/acetone (*v/v* = 19:1) at 233 K and then frozen in liquid nitrogen. Similarly intermediate **2**-Sc^{3+} was prepared by addition of $Sc(OTf)_3$ (2.0 equiv) to a reaction mixture of $Li[(TAML)Co^{III}]\cdot 3H_2O$ (2.0 mM) and PhIO (3.0 equiv) in acetone/toluene (*v/v* = 1:2) at 233 K and then frozen in liquid nitrogen. The mixed solvents were necessary for preparing glassy samples with optical transparency. By comparing UV-vis spectra before and after freezing, the equivalence of the frozen and solution samples was confirmed (Figure S31). The spectra were collected on a JASCO J1500 CD spectrometer coupled to a Cryomagnetics C-Mag Vari-7s cryomagnet, which provided a longitudinal magnetic field up to ± 7 T. Variable-temperature, variable-field MCD intensity variations were simulated by utilizing published procedures.[99,113]

Resonance Raman Spectroscopy.

A homogenous sample of intermediate **1** was prepared by the addition of $Y(OTf)_3$ (2.0 equiv) to a reaction mixture of $Li[(TAML)Co^{III}]\cdot 3H_2O$ (4.0 mM) and PhIO (3.0 equiv) in

TFE/acetone (*v/v* = 19:1) at 233 K (sample A in Figure S15a). Intermediate **2** was prepared by addition of HOTf or DOTf (5.0 equiv) to a reaction mixture of Li[(TAML)Co^{III}]•$3H_2O$ (2.0 mM) and PhIO (3.0 equiv) in acetone/toluene (*v/v* = 1:2) at temperature below 193 K (sample B_{193K}). This sample at 233 K though had contributions from both **1** and **2** (sample B_{233K}, Figure S15a). The Raman spectra collected with near-UV laser excitations were measured on an Andor SR-500i imaging spectrometer equipped with a 1800 l/mm grating, an Andor iDUS DU420A-BU2 detector, and Changchun New Industries optoelectronics 355, 405, and 442 nm lasers. The spectra measured with visible laser excitations were obtained on an Andor SR-750-A-R spectrometer equipped with a 1,200 l/mm grating, an AndoriVac DR-316B-LDCDD-RES detector, and Changchun New Industries optoelectronics 532 nm laser. The spectra obtained with near-IR laser excitations were collected with an Andor SR-303i spectrometer equipped with a 1,200 l/mm grating, an Andor iVac DR-324B-FI-RES detector, and an Innovative Photonic Solutions 830 and 633 nm lasers. The temperature of samples was controlled with a Linkam LNP96-S liquid nitrogen pump and a Linkam T96-S temperature controller.

X-ray Absorption Spectroscopy.

Intermediate **1** was prepared by the addition of $Y(OTf)_3$ (2.0 equiv) to a reaction mixture of Li[(TAML)Co^{III}]•$3H_2O$ (5.0 mM) and PhIO (3.0 equiv) in TFE/acetone (*v/v* = 19:1) at 233 K. Intermediate **2**-Sc^{3+} was prepared by addition of $Sc(OTf)_3$ (2.0 equiv) to a reaction mixture of Li[(TAML)Co^{III}]•$3H_2O$ (2.0 mM) and PhIO (3.0 equiv) in acetone at 193 K. Intermediate **2**-Y^{3+} was prepared by addition of $Y(OTf)_3$ (2.0 equiv) to a reaction mixture of Li[(TAML)Co^{III}]•$3H_2O$ (2.0 mM) and PhIO (3.0 equiv) in acetone at 193 K. Solutions were injected into aluminum sample holders between widows made from Kapton tape, and frozen in liquid nitrogen. Cobalt K-edge X-ray absorption spectra of **1** and **2** were subsequently measured at the Canadian Light Source (Saskatoon, Saskatchewan, CA) on beamline 07ID-2 (BioXAS-Spectroscopy) with temperatures maintained using an Oxford liquid He cryostat at 20 K. Spectra were collected with a 32 element solid-state Ge detector (Canberra) with an Fe-filter placed between the sample and detector and calibrated against the first inflection point of the Co-foil (7709.0 eV), which was simultaneously collected with the data. Data were collected in 10 eV steps in the far pre-edge region (7508 – 7700 eV, 1 s integration time), 0.3 eV steps in the pre-edge region (7700 – 7725 eV, 2 s integration time), 1.0 eV steps in the edge region (7725 – 7755 eV, 2 s integration time), 2.0 eV steps in the near post-edge region (7755 – 8000 eV, 3 s integration time), and 0.05 k steps in the far post edge region (8000 eV – 16.0 $Å^{-1}$, extrapolated from 3 – 9 s integration time). As a consequence of photodamage to the sample, the 1 x 1 mm beam was moved after every other scan. Total fluorescence counts were maintained under 50 kHz, and a deadtime correction yielded no change to the data. The reported spectra are the averaged spectra of either 10 (for **1**) or 6 (for **2**) individual data sets. Prior to data averaging, each spectrum and individual data channel was inspected for data quality. The reported fits are based on an analysis of the data over the range of $k = 2.2 – 15.0$ $Å^{-1}$ and are models on the unfiltered k^3 EXAFS data as previously reported.[114]

Computational Details.

This work reports on multiple sets of quantum chemical calculations that employed different levels of theory: (i) Geometry optimizations, single point energy calculations, vibrational frequency calculations and electronic absorption spectra simulations on the level of Density Functional Theory (DFT) and (ii) single-point multireference electronic structure calculations including the evaluation of molecular *g*-tensors.

(i) DFT calculations reported on in the context of rR (see Figure 9) and MCD (see Figure 8) spectra simulations were carried out with the Jaguar 9.1 suite·[115] Geometry optimizations were performed with B3LYP-D3 functional[116–121] and the 6–31G** basis set[122] for main group atoms. Co and Sc were represented using the Los Alamos LACVP basis.[123–126] Additional single-point calculations reevaluated the energies of the optimized structures on each optimized geometry with Dunning's correlation consistent triple-ζ basis set cc-pVTZ(-f),[127] which includes a double set of polarization functions. For Co and Sc, we used a modified version of LACVP, designated as LACV3P, in which the exponents were decontracted to match the effective core potential with triple-ζ quality. Solvation energies were evaluated by a self-consistent reaction field (SCRF) approach based on accurate numerical solutions of the Poisson−Boltzmann equation. In the results reported, solvation calculations were carried out with the 6–31G**/LACVP basis at the optimized gas-phase geometry employing the dielectric constants of ε = 20.7 for acetone. As is the case for all continuum models, the solvation energies are subject to empirical parametrization of the atomic radii that are used to generate the solute surface. We employed the standard set of optimized radii in Jaguar for H (1.150 Å), C (1.900 Å), N (1.600 Å), F (1.682 Å), S (1.900 Å), Sc (1.647 Å), and Co (1.436 Å). Analytical vibrational frequencies within the harmonic approximation were computed with the 6–31G**/LACVP basis to confirm proper convergence to well-defined minima or saddle points on the potential energy surface. The energy components have been computed with the following protocol. The free energy in solution-phase, G(sol), has been calculated as follows:

$$G(\text{sol}) = G(\text{gas}) + G_{\text{solv}} \tag{1}$$

$$G(\text{gas}) = H(\text{gas}) - TS(\text{gas}) \tag{2}$$

$$H(\text{gas}) = E(\text{SCF}) + \text{ZPE} \tag{3}$$

$$\Delta E(\text{SCF}) = \sum E(\text{SCF})_{\text{P}} - \sum E(\text{SCF})_{\text{R}} \tag{4}$$

$$\Delta G(\mathrm{sol}) = \sum G(\mathrm{sol})_{\mathrm{P}} - \sum G(\mathrm{sol})_{\mathrm{R}} \quad (5)$$

where $\sum E(\mathrm{SCF})_{\mathrm{P}}$ and $\sum E(\mathrm{SCF})_{\mathrm{R}}$ values indicate $\sum E(\mathrm{SCF})$ values for products and reactants, respectively, and $\sum G(\mathrm{sol})_{\mathrm{P}}$ and $\sum G(\mathrm{sol})_{\mathrm{R}}$ values indicate $\sum G(\mathrm{sol})$ values for products and reactants, respectively.

An additional set of DFT calculations on **1** and **2** was performed using the ORCA program package (version 5.0.3).[128] 2During these additional calculations the def2-TZVP basis set was used for Co, its four ligating N atoms and the axially bound O atom. For all other atoms, the def2-SVP basis set was used.[129] As in the aforementioned set of calculations, the B3LYP functional was employed. The computation of Coulomb and exchange integrals was accelerated by means of the Resolution-of-the-identity (RIJ) approximation and the chain-of-spheres (COSX) approximation, respectively (RIJCOSX).[130–134] In the context of the RIJ approximation the def2/J auxiliary basis set was utilized.[135] Solvation effects were modeled with the Conductor-like polarizable continuum model (CPCM).[136,137] DFT energies were corrected by Grimme's D3 correction with Becke-Johnson damping (D3BJ).[121] XANES spectra were simulated within the time-dependent DFT framework.[138]

(ii) All reported multireference (MR) electronic structure calculations were conducted with the ORCA program package and used the same combination of def2-TZVP, def2-SVP and def2/J basis sets outlined above. In here, we have adopted the conventional CASSCF(m,n) notation for complete active space self-consistent field calculations where m is the number of active electrons while n is the number of active orbitals. The (13, 9) active space used in this work was chosen through a combination of the ASS1ST method and chemical intuition.[139,140] The active orbitals comprise a combination of Co d-orbitals and ligand-based π orbitals (See Supporting Information). All reported CASSCF calculations incorporated 10 doublet states in a state-averaged fashion. Dynamic electron correlation effects were accounted for by the strongly contracted variant of second order N-electron valence perturbation theory (SC-NEVPT2).[141] On top of the non-relativistic CASSCF + SC-NEVPT2 calculations, spin-orbit coupling (SOC) effects were taken into account by means of a quasi-degenerate perturbation theory Ansatz in the basis of the computed 10 doublet states.[142] This approach can be regarded as a molecular equivalent to atomic Russell-Saunders coupling. During the evaluation of the SOC Hamiltonian matrix elements the spin-orbit mean field (SOMF) approximation was used.[143,144] Moreover, it should be noted that the required spin-density matrices were obtained on the CASSCF level of theory while the diagonal energies in the Born-Oppenheimer Hamiltonian matrix HBO are the SC-NEVPT2 state energies. Finally, the molecular g-tensors were computed on the basis of the lowest Kramer's doublet as described elsewhere in detail. [107,145,146]

Reactivity Studies of 1 and 2.

The kinetic experiments were run at least in triplicate, and the data reported represent the average of these reactions. Rate constants for sulfoxidation (thioanisoles) and HAT reactions (1,4-cyclohexadiene and 2,6-DTBP) were determined under pseudo-first-order conditions

(i.e., [substrate]/[intermediate] > 10) by fitting the changes in absorbance for disappearance of peaks at 600 nm due to **1** and 950 nm due to **2**. Intermediate **1** was generated by reacting Li[Co^{III}(TAML)]•$3H_2O$ (1.0 mM) with PhIO (3.0 equiv) and HOTf (5.0 equiv) in acetone at various temperature (263–233 K) and then reacted it with substrates at variable temperatures. Intermediate **2** was generated by reacting Li[Co^{III}(TAML)]•$3H_2O$ (1.0 mM) with PhIO (3.0 equiv) and HOTf (5.0 equiv) in acetone at 193 K to generate 100 % **2** and then transferred it to various temperature (233–193K) and reacted it with substrates.

Product Analysis.

Products produced in the oxidation of thioanisole, 1,4-cyclohexadiene and 2,6-DTBP by **1** and **2** were analyzed by GC. ^{18}O labelled product in sulfoxidation reactions were analyzed by GC-MS. Product yields were determined by comparing the peak areas of sample products in GC and GC-MS chromatograms against standard curves prepared with known authentic references. The inorganic cobalt products obtained in the oxidation of substrates by cobalt intermediates were also analyzed by EPR and ESI-MS spectroscopies.

Supplementary Material

Refer to Web version on PubMed Central for supplementary material.

ACKNOWLEDGMENT

This work was supported by the NRF of Korea (NRF-2021R1A3B1076539 to W.N., NRF-2023R1A2C1007668 to Y.-M.L., NRF-2023R1A2C200473311 to S.H.K., NRF-2018R1C1B6007430 to K.P.), the Institute for Basic Science in Korea (IBS-R010-A1 to M.-H.B.). G.S. and M.R. thank the German Science Foundation (DFG) for funding through grant RO 5688/3 and K.R. thanks the Deutsche Forschungsgemeinschaft (DFG) for financial support (Germany's Excellence Strategy EXC-2008-390540038-"UniSysCat" and RA 2409/11-1). J.S. thanks the NSF CHE-1900380 and NIH R15-GM141650. S.F. thanks a JSPS grant, 23K0468.

REFERENCES

(1). Lewis NS; Nocera DG Powering the Planet: Chemical Challenges in Solar Energy Utilization. Proc. Natl. Acad. Sci. USA 2006, 103, 15729–15735. [PubMed: 17043226]

(2). Ozerov OV Oxidative Addition of Water to Transition Metal Complexes. Chem. Soc. Rev 2009, 38, 83–88. [PubMed: 19088967]

(3). Gust D; Moore TA; Moore AL Solar Fuels via Artificial Photosynthesis. Acc. Chem. Res 2009, 42, 1890–1898. [PubMed: 19902921]

(4). Concepcion JJ; Tsai M-K; Muckerman JT; Meyer TJ Mechanism of Water Oxidation by Single-Site Ruthenium Complex Catalysts. J. Am. Chem. Soc 2010, 132, 1545–1557. [PubMed: 20085264]

(5). Dau H; Limberg C; Reier T; Risch M; Roggan S; Strasser P The Mechanism of Water Oxidation: From Electrolysis via Homogeneous to Biological Catalysis. ChemCatChem 2010, 2, 724–761.

(6). Artero V; Chavarot-Kerlidou M; Fontecave M Splitting Water with Cobalt. Angew. Chem., Int. Ed 2011, 50, 7238–7266.

(7). Hetterscheid DGH; Reek JNH Mononuclear Water Oxidation Catalysts. Angew. Chem., Int. Ed 2012, 51, 9740–9747.

(8). Lai W; Cao R; Dong G; Shaik S; Yao J; Chen H Why Is Cobalt the Best Transition Metal in Transition-Metal Hangman Corroles for O−O Bond Formation During Water Oxidation? J. Phys. Chem. Lett 2012, 3, 2315–2319. [PubMed: 26292109]

(9). McAlpina JG; Sticha TA; Caseya WH; Britt RD Comparison of Cobalt and Manganese in the Chemistry of Water Oxidation. Coord. Chem. Rev 2012, 256, 2445–2452.

(10). Siegbahn PEM Water Oxidation Mechanism in Photosystem II, Including Oxidations, Proton Release Pathways, O-O Bond Formation and O_2 Release. Biochim. Biophys. Acta, Bioenerg 2013, 1827, 1003–1019.

(11). Li X; Siegbahn PEM Water Oxidation Mechanism for Synthetic Co−Oxides with Small Nuclearity. J. Am. Chem. Soc 2013, 135, 13804–13813. [PubMed: 23968287]

(12). Blakemore JD; Crabtree RH; Brudvig GW Molecular Catalysts for Water Oxidation. Chem. Rev 2015, 115, 12974–13005. [PubMed: 26151088]

(13). Zhang C; Chen C; Dong H; Shen J-R; Dau H; Zhao J A Synthetic Mn_4Ca-Cluster Mimicking the Oxygen-Evolving Center of Photosynthesis. Science 2015, 348, 690–693. [PubMed: 25954008]

(14). Britt RD; Suess DLM; Stich TA An Mn(V)–Oxo Role in Splitting Water? Proc. Natl. Acad. Sci. USA 2015, 112, 5265–5266. [PubMed: 25883270]

(15). Gupta R; Taguchi T; Lassalle-Kaiser B; Bominaar EL; Yano J; Hendrich MP; Borovik AS High-Spin Mn–Oxo Complexes and Their Relevance to the Oxygen-Evolving Complex Within Photosystem II. Proc. Natl. Acad. Sci. USA 2015, 112, 5319–5324. [PubMed: 25852147]

(16). Hunter BM; Gray HB; Müller AM Earth-Abundant Heterogeneous Water Oxidation Catalysts. Chem. Rev 2016, 116, 14120–14136. [PubMed: 27797490]

(17). Fukuzumi S; Kojima T; Y.-M.; Nam, W. High-Valent Metal-Oxo Complexes Generated in Catalytic Oxidation Reactions Using Water as an Oxygen Source. Coord. Chem. Rev 2017, 333, 44–56.

(18). El-Khouly ME; El-Mohsnawy E; Fukuzumi S Solar Energy Conversion: From Natural to Artificial Photosynthesis. J. Photochem. Photobiol 2017, 31, 36–83.

(19). Xu L; Lei H; Zhang Z; Yao Z; Li J; Yua Z; Cao R The Effect of the Trans Axial Ligand of Cobalt Corroles on Water Oxidation Activity in Neutral Aqueous Solutions. Phys. Chem. Chem. Phys 2017, 19, 9755–9761. [PubMed: 28184402]

(20). Fukuzumi S; Lee Y-M; Nam W Kinetics and Mechanisms of Catalytic Water Oxidation. Dalton Trans 2019, 48, 779–798. [PubMed: 30560964]

(21). Li X; Zhang X-P; Guo M; Lv B; Guo K; Jin X; Zhang W; Lee Y-M; Fukuzumi S; Nam W; Cao R Identifying Intermediates in Electrocatalytic Water Oxidation with a Manganese Corrole Complex. J. Am. Chem. Soc 2021, 143, 14613–14621. [PubMed: 34469154]

(22). Chattopadhyay S; Ghatak A; Ro Y; Guillot R; Halime Z; Aukauloo A; Dey A Ligand Radical Mediated Water Oxidation by a Family of Copper *o*-Phenylene Bis-oxamidate Complexes. Inorg. Chem 2021, 60, 9442–9455. [PubMed: 34137590]

(23). Chen Q-F; Guo Y-H; Yu Y-H; Zhang M-T Bioinspired Molecular Clusters for Water Oxidation. Coord. Chem. Rev 2021, 448, No. 214164.

(24). Parenta AR; Nakazonob T; Tsubonouchic Y; Tairad N; Sakai K Mechanisms of Water Oxidation Using Ruthenium, Cobalt, Copper, and Iron Molecular Catalysts. Adv. Inorg. Chem 2019, 74, 197–240.

(25). Matheu R; Garrido-Barros P; Gil- Sepulcre M; Ertem MZ; Sala X; Gimbert-Suriñach C; Llobet A The Development of Molecular Water Oxidation Catalysts. Nat. Rev. Chem 2019, 3, 331–341.

(26). Hong YH; Han JW; Jung J; Nakagawa T; Lee Y-M; Nam W; Fukuzumi S Photocatalytic Oxygenation Reactions with a Cobalt Porphyrin Complex Using Water as an Oxygen Source and Dioxygen as an Oxidant. J. Am. Chem. Soc 2019, 141, 9155–9159. [PubMed: 31145595]

(27). Hong YH; Lee Y-M; Nam W; Fukuzumi S Molecular Photocatalytic Water Splitting by Mimicking Photosystems I and II. J. Am. Chem. Soc 2022, 144, 695–700. [PubMed: 34990144]

(28). Chen X; Guo R.-t.; Hong L.-f.; Yuan Y; Pan W.-g. Research Progress on CO_2 Photocatalytic Reduction with Full Solar Spectral Responses. Energy Fuels 2021, 35, 19920–19942.

(29). Yoshino S; Takayama T; Yamaguchi Y; Iwase A; Kudo A CO_2 Reduction Using Water as an Electron Donor over Heterogeneous Photocatalysts Aiming at Artificial Photosynthesis. Acc. Chem. Res 2022, 55, 966–977. [PubMed: 35230087]

(30). Wu Z; Yang Q; Liu Y; Zhang B; Li R; Wang W; Wang J; Domen K; Wang F; Fan F Can Li: A Career in Catalysis. ACS Catal 2022, 12, 3063–3082.

(31). Song H; Luo S; Huang H; Deng B; Ye J Solar-Driven Hydrogen Production: Recent Advances, Challenges, and Future Perspectives. ACS Energy Lett 2022, 7, 1043–1065.

(32). Kim S; Kim KH; Oh C; Zhang K; Park JH Artificial Photosynthesis for High-Value-Added Chemicals: Old Material, New Opportunity. Carbon Energy 2022, 4, 21–44.

(33). Chatenet M; Pollet BG; Dekel DR; Dionigi de F.; Deseure J; Millet P; Braatz RD; Bazant MZ; Eikerling M; Staffell I; Balcombe P; Shao-Horn Y; Schafer H Water Electrolysis: From Textbook Knowledge to the Latest Scientific Strategies and Industrial Developments. Chem. Soc. Rev 2022, 51, 4583–4762. [PubMed: 35575644]

(34). Tao X; Zhao Y; Wang S; Li C; Li R Recent Advances and Perspectives for Solar-Driven Water Splitting Using Particulate Photocatalysts. Chem. Soc. Rev 2022, 51, 3561–3608. [PubMed: 35403632]

(35). Samanta B; Morales-García Á; Illas F; Goga N; Anta JA; Calero S; Bieberle-Hütter A; Libisch F; Muñoz-García AB; Pavone M; Toroker MC Challenges of Modeling Nanostructured Materials for Photocatalytic Water Splitting. Chem. Soc. Rev 2022, 51, 3794–3818. [PubMed: 35439803]

(36). McAlpin JG; Surendranath Y; Dinca M; Stich TA; Stoian SA; Casey WH; Nocera DG; Britt RD EPR Evidence for Co(IV) Species Produced During Water Oxidation at Neutral pH. J. Am. Chem. Soc 2010, 132, 6882–6883. [PubMed: 20433197]

(37). Wasylenko DJ; Ganesamoorthy C; Borau-Garcia J; Berlinguette CP Electrochemical Evidence for Catalytic Water Oxidation Mediated by a High-Valent Cobalt Complex. Chem. Commun 2011, 47, 4249–4251.

(38). Wasylenko DJ; Palmer RD; Schottb E; Berlinguette CP Interrogation of Electrocatalytic Water Oxidation Mediated by a Cobalt Complex. Chem. Commun 2012, 48, 2107–2109.

(39). Wang D; Groves JT Efficient Water Oxidation Catalyzed by Homogeneous Cationic Cobalt Porphyrins with Critical Roles for the Buffer Base. Proc. Natl. Acad. Sci. USA 2013, 110, 15579–15584. [PubMed: 24019473]

(40). Das D; Pattanayak S; Singh KK; Garaib B; Gupta SS Electrocatalytic Water Oxidation by a Molecular Cobalt Complex Through a High Valent Cobalt Oxo Intermediate. Chem. Commun 2016, 52, 11787–11790.

(41). Swierk JR; Tilley TD Electrocatalytic Water Oxidation by Single Site and Small Nuclearity Clusters of Cobalt. J. Electrochem. Soc 2018, 165, H3028–H3033.

(42). Du H-Y; Chen S-C; Su X-J; Jiao L; Zhang M-T Redox-Active Ligand Assisted Multielectron Catalysis: A Case of Co^{III} Complex as Water Oxidation Catalyst. J. Am. Chem. Soc 2018, 140, 1557–1565. [PubMed: 29309165]

(43). Sinha W; Mizrahi A; Mahammed A; Tumanskii B; Gross Z Reactive Intermediates Involved in Cobalt Corrole Catalyzed Water Oxidation (and Oxygen Reduction). Inorg. Chem 2018, 57, 478–485. [PubMed: 29256608]

(44). McMillion ND; Wilson AW; Goetz MK; Chang M-C; Lin C-C; Feng W-J; McCrory CCL; Anderson JS Imidazole for Pyridine Substitution Leads to Enhanced Activity Under Milder Conditions in Cobalt Water Oxidation Electrocatalysis. Inorg. Chem 2019, 58, 1391–1397. [PubMed: 30589548]

(45). Biswas S; Bose S; Debgupta J; Dasd P; Biswas AN Redox-Active Ligand Assisted Electrocatalytic Water Oxidation by a Mononuclear Cobalt Complex. Dalton Trans 2020, 49, 7155–7165. [PubMed: 32412571]

(46). Neuman NI; Albold U; Ferretti E; Chandra S; Steinhauer S; Rößner P; Meyer F; Doctorovich F; Vaillard SE; Sarkar B Cobalt Corroles as Electrocatalysts for Water Oxidation: Strong Effect of Substituents on Catalytic Activity. Inorg. Chem 2020, 59, 16622–16634. [PubMed: 33153263]

(47). Das PK; Bhunia S; Chakraborty P; Chatterjee S; Rana A; Peramaiah K; Alsabban MM; Dutta I; Dey A Huang K-W Electrocatalytic Water Oxidation by a Phosphorus−Nitrogen O=PN3– Pincer Cobalt Complex. Inorg. Chem 2021, 60, 614–622. [PubMed: 33236627]

(48). Xie F; Zhang M-T Bimetallic Water Oxidation: One-Site Catalysis with Two-Sites Oxidation. J. Energy Chem 2021, 63, 1–7.

(49). Zhang X; Chen Q-F; Deng J; Xu X; Zhan J; Du H-Y; Yu Z; Li M; Zhang M-T; Shao Y Identifying Metal-Oxo/Peroxo Intermediates in Catalytic Water Oxidation by In Situ Electrochemical Mass Spectrometry. J. Am. Chem. Soc 2022, 144, 17748–17752. [PubMed: 36149317]

(50). Su Y-F; Luo W-Z; Lin W-Q; Su Y-B; Li Z-J; Yuan Y-J; Li J-F; Chen G-H; Li Z; Yu Z-T; Zou Z A Water-Soluble Highly Oxidizing Cobalt Molecular Catalyst Designed for Bioinspired Water Oxidation. Angew. Chem., Int. Ed 2022, 61, No. e202201430.

(51). Gerken JB; McAlpin JG; Chen JYC; Rigsby ML; Casey WH; Britt RD; Stahl SS Electrochemical Water Oxidation with Cobalt-Based Electrocatalysts from pH 0–14: The Thermodynamic Basis for Catalyst Structure, Stability, and Activity. J. Am. Chem. Soc 2011, 133, 14431–14442. [PubMed: 21806043]

(52). Nakazono T; Parenta AR; Sakai K Cobalt Porphyrins as Homogeneous Catalysts for Water Oxidation. Chem. Commun 2013, 49, 6325–6327.

(53). Das B; Orthaber A; Ott S; Thapper A Water Oxidation Catalysed by a Mononuclear Co^{II} Polypyridine Complex; Possible Reaction Intermediates and the Role of the Chloride Ligand. Chem. Commun 2015, 51, 13074–13077.

(54). Wang N; Zheng H; Zhang W; Cao R Mononuclear First-Row Transition-Metal Complexes as Molecular Catalysts for Water Oxidation. Chin. J. Catal 2018, 39, 228–244.

(55). Mondal B; Chattopadhyay S; Dey S; Mahammed A; Mittra K; Rana A; Gross Z; Dey A Elucidation of Factors that Govern the $2e^-/2H^+$ vs $4e^-/4H^+$ Selectivity of Water Oxidation by a Cobalt Corrole. J. Am. Chem. Soc 2020, 142, 21040–21049. [PubMed: 33259190]

(56). Li F; Yu F; Wang X; Zhou X; Li H; Jiang Y; Sun L Electrochemical and Photoelectrochemical Water Oxidation by Supported Cobalt−Oxo Cubanes. ACS Catal 2014, 4, 804–809.

(57). Nguyen AI; Wang J; Levine DS; Ziegler MS; Tilley TD Synthetic Control and Empirical Prediction of Redox Potentials for Co_4O_4 Cubanes over a 1.4 V Range: Implications for Catalyst Design and Evaluation of High-Valent Intermediates in Water Oxidation. Chem. Sci 2017, 8, 4274–4284. [PubMed: 29081963]

(58). Amtawong J; Nguyen AI; Tilley TD Mechanistic Aspects of Cobalt–Oxo Cubane Clusters in Oxidation Chemistry. J. Am. Chem. Soc 2022, 144, 1475–1492. [PubMed: 35060704]

(59). Betley TA; Wu Q; Voorhis TV; Nocera DG Electronic Design Criteria for O−O Bond Formation via Metal−Oxo Complexes. Inorg. Chem 2008, 47, 1849–1861. [PubMed: 18330975]

(60). Winkler JR; Gray HB Electronic Structures of Oxo-Metal Ions. Struct Bond 2012, 142, 17–28.

(61). Gray HB; Winkler JR Living with Oxygen. Acc. Chem. Res 2018, 51, 1850–1857. [PubMed: 30016077]

(62). Larson VA; Battistella B; Ray K; Lehnert N; Nam W Iron and Manganese Oxo Complexes, Oxo Wall and Beyond. Nat. Rev. Chem 2020, 4, 404–419. [PubMed: 37127969]

(63). Karmalkar DG; Larson VA; Malik DD; Lee Y-M; Seo MS; Kim J; Vasiliauskas D; Shearer J; Lehnert N; Nam W Preparation and Characterization of a Formally Ni^{IV}–Oxo Complex with a Triplet Ground State and Application in Oxidation Reactions. J. Am. Chem. Soc 2022, 144, 22698–22712. [PubMed: 36454200]

(64). Zhang X-P; Chandra A; Lee Y-M; Cao R; Ray K; Nam W Transition Metal-Mediated O–O Bond Formation and Activation in Chemistry and Biology. Chem. Soc. Rev 2021, 50, 4804–4811. [PubMed: 33657202]

(65). Wang B; Lee Y-M; Tcho W-Y; Tussupbayev S; Kim S-T; Kim Y; Seo MS; Cho K-B; Dede Y; Keegan BC; Ogura T; Kim SH; Ohta T; Baik M-H; Ray K; Shearer J; Nam W Synthesis and Reactivity of a Mononuclear Non-Haem Cobalt(IV)-Oxo Complex. Nat. Commun 2017, 8, No. 14839. [PubMed: 28337985]

(66). Yang J; Dong HT; Seo MS; Larson VA; Lee Y-M; Shearer J; Lehnert N; Nam W The Oxo-Wall Remains Intact: A Tetrahedrally Distorted Co(IV)–Oxo Complex. J. Am. Chem. Soc 2021, 143, 16943–16959. [PubMed: 34609879]

(67). (a) Pfaff FF; Kundu S; Risch M; Pandian S; Heims F; Pryjomska-Ray I; Haack P; Metzinger R; Bill E; Dau H; Comba P; Ray K An Oxocobalt(IV) Complex Stabilized by Lewis Acid Interactions with Scandium(III) Ions. Angew. Chem., Int. Ed 2011, 50, 1711–1715;(b) Malik DD; Chandra A; Seo MS; Lee Y-M; Farquhar ER; Mebs S; Dau H; Ray K; Nam W Formation of Cobalt–Oxygen Intermediates by Dioxygen Activation at a Mononuclear Nonheme Cobalt(II) Center. Dalton Trans 2021, 50, 11889–11898. [PubMed: 34373886]

(68). Lacy DC; Park YJ; Ziller JW; Yano J; Borovik AS Assembly and Properties of Heterobimetallic $Co^{II/III}/Ca^{II}$ Complexes with Aquo and Hydroxo Ligands. J. Am. Chem. Soc 2012, 134, 17526–17535. [PubMed: 22998407]

(69). Hong S; Pfaff FF; Kwon E; Wang Y; Seo M-S; Bill E; Ray K; Nam W Spectroscopic Capture and Reactivity of a Low-Spin Cobalt(IV)-Oxo Complex Stabilized by Binding Redox-Inactive Metal Ions. Angew. Chem., Int. Ed 2014, 53, 10403–10407.

(70). Hong S; Pfaff FF; Kwon E; Wang Y; Seo M-S; Bill E; Ray K; Nam W Spectroscopic Capture and Reactivity of a Low-Spin Cobalt(IV)-Oxo Complex Stabilized by Binding Redox-Inactive Metal Ions. Corrigendum: Angew. Chem., Int. Ed 2017, 56, 10630–10630.

(71). (a) Collins TJ; Powell RD; Slebodnick C; Uffelman ES Stable Highly Oxidizing Cobalt Complexes of Macrocyclic Ligands. J. Am. Chem. Soc 1991, 113, 8419–8425.(b) Collins TJ; Uffelman ES The First Macrocyclic Square-Planar Cobalt(r1r) Complex Relieves Ring Strain by Forming a Nonplanar Amide. Angew. Chem., Int. Ed 2017, 28, 1509–1511. (c) Note in Scheme 2 that the fused phenyl ring of this TAML variant is crucial as it allows for ligand non-innocence. TAML macrocycles absent this moiety, such as TAMLR = [(Me2CNCOCMe2NCO)2CMe2]4− as shown in Figure S32, do not support the oxidized cobalt.

(72). Popescu D-L; Chanda A; Stadler M; de Oliveira FT; Ryabov AD; Munck E; Bominaar EL; Collins TJ High-Valent First-Row Transition-Metal Complexes of Tetraamido (4N) and Diamidodialkoxido or Diamidophenolato (2N/2O) Ligands: Synthesis, Structure, and Magnetochemistry. Coord. Chem. Rev 2008, 252, 2050–2071.

(73). (a) van Leest NP; Tepaske MA; Oudsen J-PH; Venderbosch B; Rietdijk NR; Siegler MA; Tromp M; van der Vlugt JI; de Bruin B Ligand Redox Noninnocence in [CoIII(TAML)]0/− Complexes Affects Nitrene Formation. J. Am. Chem. Soc 2020, 142, 552–563. [PubMed: 31846578] (b) van Leest NP; Tepaske MA; Venderbosch B; Oudsen J-PH; Tromp M; van der Vlugt JI; de Bruin B Electronically Asynchronous Transition States for C−N Bond Formation by Electrophilic [CoIII(TAML)]– Nitrene Radical Complexes Involving Substrate-to-Ligand Single-Electron Transfer and a Cobalt-Centered Spin Shuttle. ACS Catal 2020, 10, 7449–7463. [PubMed: 35912398]

(74). van Leest NP; van der Vlugt JI; de Bruin B Catalytic Chemoselective Sulfimidation with an Electrophilic [CoIII(TAML)]– Nitrene Radical Complex. Chem. – Eur. J 2021, 27, 371–378. [PubMed: 32810326]

(75). van Leest NP; de Zwart FJ; Zhou M; de Bruin B Controlling Radical-Type Single-Electron Elementary Steps in Catalysis with Redox-Active Ligands and Substrates. J. Am. Chem. Soc. Au 2021, 1, 1101–1115.

(76). Malik DD; Lee Y-M; Nam W Identification of a Cobalt(IV)–Oxo Intermediate as an Active Oxidant in Catalytic Oxidation Reactions. Bull. Korean Chem. Soc 2022, 43, 1075–1082.

(77). Que L Jr. Physical Methods in Bioinorganic Chemistry: Spectroscopy and Magnetism; University Science Books, Sausalito, 2000.

(78). Yin G Active Transition Metal Oxo and Hydroxo Moieties in Nature's Redox, Enzymes and Their Synthetic Models: Structure and Reactivity Relationships. Coord. Chem. Rev 2010, 254, 1826–1842.

(79). Yin G Understanding the Oxidative Relationships of the Metal Oxo, Hydroxo, and Hydroperoxide Intermediates with Manganese(IV) Complexes Having Bridged Cyclams: Correlation of the Physicochemical Properties with Reactivity. Acc. Chem. Res 2013, 46, 483–492. [PubMed: 23194251]

(80). Liu Y; Lau T-C Activation of Metal Oxo and Nitrido Complexes by Lewis Acids. J. Am. Chem. Soc 2019, 141, 3755–3766. [PubMed: 30707842]

(81). Rice DB; Grotemeyer EN; Donovan AM; Jackson TA Effect of Lewis Acids on the Structure and Reactivity of a Mononuclear Hydroxomanganese(III) Complex. Inorg. Chem 2020, 59, 2689–2700. [PubMed: 32045220]

(82). Karmalkar DG; Seo MS; Lee Y-M; Kim Y; Lee E; Sarangi R; Fukuzumi S; Nam W Deeper Understanding of Mononuclear Manganese(IV)−Oxo Binding Brønsted and Lewis Acids and the Manganese(IV)−Hydroxide Complex. Inorg. Chem 2021, 60, 16996–17007. [PubMed: 34705465]

(83). Saracini C; Malik DD; Sankaralingam M; Lee Y-M; Nam W; Fukuzumi S Enhanced Electron-Transfer Reactivity of a Long-Lived Photoexcited State of a Cobalt−Oxygen Complex. Inorg. Chem 2018, 57, 10945–10952. [PubMed: 30133298]

(84). The blue species assigned as [(TAML•+)CoIII(OH)]– in Scheme 2 can be produced by electron transfer (ET) from Li[(TAML)CoIII]•3H2O to one-electron oxidants, such as [cerium(IV) ammonium nitrate (CAN), CuII(OTf), tris(4-bromophenyl)ammoniumyl radical cation (TBPA•+), and [Fe(bpy)3]3+ (bpy = 2,2'-bipyridine)], to produce [(TAML•+)CoIII] (or [(TAML)CoIV]), which reacts with H2O to produce the blue species ([(TAML•+)CoIII(OH)]–).69,83 Although no reaction occurs between [(TAML)CoIII]– and PhIO without acid, addition of a Lewis acid (e.g., HOTf) results in the acid-promoted ET from [(TAML)CoIII]– to PhIO to produce PhIOH• and [(TAML•+)CoIII] (or [(TAML)CoIV]) that reacts with H2O to produce [(TAML•+)CoIII(OH)]–. This is followed by a rapid acid-promoted ET from [(TAML)CoIII]– to PhIOH• to produce PhI, H2O, and [(TAML•+)CoIII] (or [(TAML)CoIV]) that further reacts with H2O to yield another [(TAML•+)CoIII(OH)]–. The overall reaction is 2[(TAML)CoIII] + PhIO + H2O 2[(TAML•+)CoIII(OH)]– + PhI, in which a Lewis acid (LA) may interact with the OH group of the blue species and H+ is not involved in the stoichiometry, acting as a catalyst to promote ET. In fact, only 0.5 equiv of PhIO is required to produce 100% yield of [(TAML•+)CoIII(OH)]– by the reaction of Li[(TAML)CoIII]•3H2O with PhIO and HOTf (SI, Figure S33).

(85). It was reported that iron(IV)-oxo complexes prohibited the ligand dissociation because of the strong binding of iron(IV) with the ligand; see Hong D; Mandal S; Yamada Y; Lee Y-M; Nam W; Llobet A; Fukuzumi S Water Oxidation Catalysis with Nonheme Iron Complexes under Acidic and Basic Conditions: Homogeneous or Heterogeneous? Inorg. Chem 2013, 52, 9522–9531. [PubMed: 23895380]

(86). Fukuzumi S; Miyamoto K; Suenobu T; Caemelbecke VE; Kadish KM Electron Transfer Mechanism of Organocobalt Porphyrins. Site of Electron Transfer, Migration of Organic Groups, and Cobalt-Carbon Bond Energies in Different Oxidation States. J. Am. Chem. Soc 1998, 120, 2880–2889.

(87). Ohkubo K; Fukuzumi S Electron-Transfer Oxidation of Coenzyme B12 Model Compounds and Facile Cleavage of the Cobalt(IV)-Carbon Bond via Charge-Transfer Complexes with Bases. A Negative Temperature Dependence of the Rates. J. Phys. Chem. A 2005, 109, 1105–1113. [PubMed: 16833419]

(88). Topich J; Halpern J Organobis(dioximato)Cobalt(IV) Complexes: Electron Paramagnetic Resonance Spectra and Electronic Structures. Inorg. Chem 1979, 18, 1339–1343.

(89). Vol'pin ME; Levitin IY; Sigan AL; Nikitaev AT Current State of Organocobalt(IV) and Organorhodium(IV) Chemistry. J. Organomet. Chem 1985, 279, 263–280.

(90). Guo M; Seo MS; Lee Y-M; Fukuzumi S; Nam W Highly Reactive Manganese(IV)-Oxo Porphyrins Showing Temperature-Dependent Reversed Electronic Effect in C−H Bond Activation Reactions. J. Am. Chem. Soc 2019, 141, 12187–12191. [PubMed: 31337211]

(91). Shadle SE; Penner-Hahn JE; Schugar HJ; Hedman B; Hodgson KO; Solomon EI X-Ray Absorption Spectroscopic Studies of the Blue Copper Site: Metal and Ligand K-Edge Studies to Probe the Origin of the EPR Hyperfine Splitting in Plastocyanin. J. Am. Chem. Soc 1993, 115, 767–776.

(92). Krewald V; Lassalle-Kaiser B; Boron TT; Pollock CJ;Kern J; Beckwith MA; Yachandra VK; Pecoraro VL; Yano J; Neese F; DeBeer S The Protonation States of Oxo-Bridged Mn^{IV} Dimers Resolved by Experimental and Computational Mn K Pre-Edge X-ray Absorption Spectroscopy. Inorg. Chem 2013, 52, 12904–12914. [PubMed: 24161030]

(93). We cannot rule out a quasi-6-coordinate species with a long (>2.5 Å) disordered axial light-atom scattered; see Supporting Information.

(94). Astashkin AV; Neese F; Raitsimring AM; Cooney JJA; Bultman E; Enemark JH Pulsed EPR Investigations of Systems Modeling Molybdenum Enzymes: Hyperfine and Quadrupole Parameters of Oxo-17O in [Mo17O(SPh)4]–. J. Am. Chem. Soc 2005, 127, 16713–16722. [PubMed: 16305262]

(95). Astashkin AV; Feng C; Raitsimring AM; Enemark JH ^{17}O ESEEM Evidence for Exchange of the Axial Oxo Ligand in the Molybdenum Center of the High pH Form of Sulfite Oxidase. J. Am. Chem. Soc 2005, 127, 502–503. [PubMed: 15643856]

(96). Astashkin AV; Johnson-Winters K; Klein EL; Feng C; Wilson HL; Rajagopalan KV; Raitsimring AM; Enemark JH Structural Studies of the Molybdenum Center of the Pathogenic R160Q Mutant of Human Sulfite Oxidase by Pulsed EPR Spectroscopy and ^{17}O and ^{33}S Labeling. J. Am. Chem. Soc 2008, 130, 8471–8480. [PubMed: 18529001]

(97). Kim Y; Kim J; Nguyen LK; Lee Y-M; Nam W; Kim SH EPR Spectroscopy Elucidates the Electronic Structure of [FeV(O)(TAML)] Complexes. Inorg. Chem. Front 2021, 8, 3775–3783.

(98). We have performed 1H/2H ENDOR to examine whether an exchangeable proton was present; however, we could not observe exchangeable proton(s), which excludes the possibility of the presence of a hydroxyl ligand (Figure S34 in SI).

(99). Neese F; Solomon EI MCD C-Term Signs, Saturation Behavior, and Determination of Band Polarizations in Randomly Oriented Systems with Spin S ≥ 1/2. Applications to S = 1/2 and S = 5/2. Inorg. Chem 1999, 38, 1847–1865. [PubMed: 11670957]

(100). (a) Ray K; Begum A; Weyhermüller T; Piligkos S; van Slageren J; Neese F; Wieghardt K The Electronic Structure of the Isoelectronic, Square-Planar Complexes [FeII(L)2]2– and [CoIII(LBu)2]– (L2– and (LBu)2– = Benzene-1,2-Dithiolates): An Experimental and Density Functional Theoretical Study. J. Am. Chem. Soc 2005, 127, 4403–4415. [PubMed: 15783223] (b) Steele J; Tahsini L; Sun C; Elinburg J; Kotyk C; McNeely J; Stoian S; Dragulescu-Andrasi A; Ozarowski A; Ozerov M; Krzystek J; Telser J; Bacon J; Golen J; Rheingold A; Doerrer L Square-Planar Co(III) in {O4} Coordination: Large ZFS and Reactivity with ROS. Chem. Commun 2018, 54, 12045–12048.(c)Birker P; Bour J; Steggerda J Spin-Triplet Cobalt Complexes of Biuret and Related Ligands. Inorg. Chem 1973, 12, 1254–1259.

(101). It is important to note that although the influence of Lewis/Brønsted acids in the stabilization of 1 and 2 have been unambiguously established, we do not exactly know the coordination environment of Sc3+ ion in 1 and 2, which will influence the total charge of the molecule. In the absence of a crystal structure, it is not possible to determine the coordination environment of Sc3+ ion experimentally based on the available spectroscopic techniques. In our DFT and multireference calculations, we have approximated the Sc3+ ion environment to contain two acetonitrile, two methanol and one triflate in both 1 and 2. This choice was inspired by the mass spectrum of 2. Please note that under the conditions of CSI-MS, complex 2 loses one proton bound to TAML and simultaneously gets reduced by one-electron to be observed as [(TAML)Co(16O)(Sc)(CH3CN)2(CH3OH)2(CF3SO3)]– (m/z = 785.1057) or as [(TAML)Co(16O)(Sc)(CH3CN)4-(CF3SO3)]– (m/z = 803.1064) after additional replacement of two CH3OH molecules by solvent CH3CN. In contrast, the CSI-MS spectrum of 1 could only be observed in the presence of Brønsted acid (i.e., HOTf) and showed a signal corresponding to the [(TAML)Co(16O)(H)]+ ion in the positive-ion mode. Please note that the deprotonation and the reduction processes observed under the CSI-MS conditions are not unexpected, in particular, when we deal with a highly unstable complex with a formal Co(IV) oxidation state as in 1 and 2.

(102). The large difference in the pre-edge intensities of 1 and 2 and the observed g-tensors in the EPR spectra can only be explained on the basis of a five-coordinate geometry in 2 and a six coordinate geometry, with a weakly bound solvent molecule, in 1. DFT calculations show that acetone binding to the Co center in 2 should lead to a significantly depleted pre-edge intensity and elongated Co-O distance, which are not consistent with the experimental results. Notably, the experimentally observed short Co=O bond at ~1.70 Å in 2, will lead to a strong trans-effect that may prevent the binding of the already weak acetone ligand in the axial position. Furthermore, the distortion of the TAML ligand associated with the protonation event, together with the site of the proton binding, may contribute to the non-binding of the solvent molecule to the Co center. However, the exact reason is not clear at this point and is beyond the scope of the present manuscript.

(103). Green MT Application of Badger's Rule to Heme and Non-Heme Iron-Oxygen Bonds: An Examination of Ferryl Protonation States. J. Am. Chem. Soc 2006, 128, 1902–1906. [PubMed: 16464091]

(104). Gordon JB; Vilbert AC; DiMucci IM; MacMillan SN; Lancaster KM; Moënne-Loccoz P; Goldberg DP Activation of Dioxygen by a Mononuclear Nonheme Iron Complex: Sequential

Peroxo, Oxo, and Hydroxo Intermediates. J. Am. Chem. Soc 2019, 141, 17533–17547. [PubMed: 31647656]

(105). Deutscher J; Gerschel P; Warm K; Kuhlmann U; Mebs S; Haumann M; Dau H; Hildebrandt P; Apfel U-P; Ray K A Bioinspired Oxoiron(IV) Motif Supported on a N2S2 Macrocyclic Ligand. Chem. Commun 2021, 57, 2947–2950.

(106). Meeus EJ; Derks MTGM; van Leest NP; Verhoef CJ; Roithová J; Reek JNH; de Bruin B Styrene Aziridination with [CoIII(TAMLred)]– in Water: Understanding and Preventing Epoxidation via Nitrene Hydrolysis. Chem Catal 2023, 3, 100712.

(107). McNaughton RL; Roemelt M; Chin JM; Schrock RR; Neese F; Hoffman BM Experimental and Theoretical EPR Study of Jahn-Teller-Active [HIPTN$_3$N]MoL Complexes (L = N2, CO, NH3). J. Am. Chem. Soc 2010, 132, 8645–8656. [PubMed: 20429559]

(108). Lee Y-M; Kim S; Ohkubo K; Kim K-H; Nam W; Fukuzumi S Unified Mechanism of Oxygen Atom Transfer and Hydrogen Atom Transfer Reactions with a Triflic Acid-Bound Non-heme Manganese(IV)−Oxo Complex via Outer-Sphere Electron Transfer. J. Am. Chem. Soc 2019, 141, 2614–2622110. [PubMed: 30646680]

(109). Sankaralingam M; Lee Y-M; Pineda-Galvan Y; Karmalkar DG; Seo MS; Jeon SH; Pushkar Y; Fukuzumi S; Nam W Redox Reactivity of a Mononuclear Manganese-Oxo Complex Binding Calcium Ion and Other Redox-Inactive Metal Ions. J. Am. Chem. Soc 2019, 141, 1324–1336. [PubMed: 30580510]

(110). Armarego WLF; Chai CLL Purification of Laboratory Chemicals. 6th edn. Pergamon Press: Oxford; U.K., 2009.

(111). Horwtiz CP; Ghosh A Synthesis of Macrocyclic Tetraamido Compounds and New Metal Insertion Process. US Patent 7060818, 2006.

(112). Saltzman H; Sharefkin JG Organic Syntheses, Collective Vol. V, Wiley: New York, 1973, p 658.

(113). Stoll S; Schweiger A Easyspin: A Comprehensive Software Package for Spectral Simulation and Analysis in EPR. J. Magn. Reson 2006, 178, 42–55. [PubMed: 16188474]

(114). Chimera is developed by the Resource for Biocomputing, Visualization, and Informatics at the University of California, San Francisco (supported by NIGMS P41-GM103311).

(115). Yang J; Seo MS; Kim KH; Lee Y-M; Fukuzumi S; Shearer J; Nam W Structure and Unprecedented Reactivity of a Mononuclear Nonheme Cobalt(III)-Iodosylbenzene Complex. Angew. Chem., Int. Ed 2020, 59, 13581–13585.

(116). Bochevarov AD; Harder E; Hughes TF; Greenwood JR; Braden DA; Philipp DM; Rinaldo D; Halls MD; Zhang J; Friesner RA Jaguar: A High-Performance Quantum Chemistry Software Program with Strengths in Life and Materials Sciences. Int. J. Quantum Chem 2013, 113, 2110–2142.

(117). Slater JC; Phillips JC Quantum Theory of Molecules and Solids Vol. 4: The Self-Consistent Field for Molecules and Solids. Phys. Today 1974, 27, 49–50.

(118). Vosko SH; Wilk L; Nusair M Accurate Spin-Dependent Electron Liquid Correlation Energies for Local Spin Density Calculations: A Critical Analysis. Can. J. Phys 1980, 58, 1201–1211.

(119). Becke AD Density-Functional Exchange-Energy Approximation with Correct Asymptotic Behavior. Phys. Rev. A 1988, 38, 3098–3100.

(120). Lee C; Yang W; Parr RG Development of the Colle-Salvetti Correlation-Energy Formula into a Functional of the Electron Density. Phys. Rev. B 1988, 37, 785–789.

(121). Becke AD Assertion and Validation of the Performance of the B3LYP* Functional for the First Transition Metal Row and the G$_2$ Test Set. J. Chem. Phys 2002, 117, 4729–4737.

(122). Grimme S; Antony J; Ehrlich S; Krieg H A Consistent and Accurate Ab Initio Parametrization of Density Functional Dispersion Correction (DFT-D) for the 94 Elements H-Pu. J. Chem. Phys 2010, 132, No. 154104. [PubMed: 20423165]

(123). Ditchfield R; Hehre WJ; Pople JA Self-Consistent Molecular-Orbital Methods. IX. An Extended Gaussian-Type Basis for Molecular-Orbital Studies of Organic Molecules. J. Chem. Phys 1971, 54, 724–728.

(124). Hay PJ; Wadt WR Ab Initio Effective Core Potentials for Molecular Calculations. Potentials for K to Au Including the Outermost Core Orbitals. J. Chem. Phys 1985, 82, 299–310.

(125). Wadt WR; Hay PJ *Ab Initio* Effective Core Potentials for Molecular Calculations. Potentials for Main Group Elements Na to Bi. J. Chem. Phys 1985, 82, 284–298.

(126). Hay PJ; Wadt WR *Ab initio* Effective Core Potentials for Molecular Calculations. Potentials for the Transition Metal Atoms Sc to Hg. J. Chem. Phys 1985, 82, 270–283.

(127). Dunning TH Gaussian Basis Sets for Use in Correlated Molecular Calculations. I. The Atoms Boron through Neon and Hydrogen. J. Chem. Phys 1989, 90, 1007–1023.

(128). Neese F; Wennmohs F; Becker U; Riplinger C The ORCA Quantum Chemistry Program Package. J. Chem. Phys 2020, 152, No. 224108. [PubMed: 32534543]

(129). Weigend F; Ahlrichs R Balanced Basis Sets of Split Valence, Triple Zeta Valence and Quadruple Zeta Valence Quality for H to Rn: Design and Assessment of Accuracy. Phys. Chem. Chem. Phys 2005, 7, 3297–3305. [PubMed: 16240044]

(130). Dunlap BI; Connolly JWD; Sabin JR On Some Approximations in Applications of $X\alpha$ Theory. J. Chem. Phys 1979, 71, 3396–3402.

(131). Vahtras O; Almlöf J; Feyereisen MW Integral Approximations for LCAO-SCF Calculations. Chem. Phys. Lett 1993, 213, 514–518.

(132). Neese F; Wennmohs F; Hansen A; Becker U Efficient, Approximate and Parallel Hartree–Fock and Hybrid DFT Calculations. A 'Chain-of-Spheres' Algorithm for the Hartree–Fock Exchange. Chem. Phys 2009, 356, 98–109.

(133). Izśak R; Neese F An Overlap Fitted Chain of Spheres Exchange Method. J. Chem. Phys 2011, 135, No. 144105. [PubMed: 22010696]

(134). Izśak R; Neese F; Klopper W Robust Fitting Techniques in the Chain of Spheres Approximation to the Fock Exchange: The Role of the Complementary Space. J. Chem. Phys 2013, 139, No. 094111. [PubMed: 24028106]

(135). Weigend F Accurate Coulomb-Fitting Basis Sets for H to Rn. Phys. Chem. Chem. Phys 2006, 8, 1057–1065. [PubMed: 16633586]

(136). Barone V; Cossi M Quantum Calculation of Molecular Energies and Energy Gradients in Solution by a Conductor Solvent Model. J. Phys. Chem. A 1998, 102, 1995–2001.

(137). Garcia-Raťes M; Neese F Effect of the Solute Cavity on the Solvation Energy and Its Derivatives within the Framework of the Gaussian Charge Scheme. J. Comp. Chem 2020, 41, 922–939. [PubMed: 31889331]

(138). Roemelt M; Beckwith MA; Duboc C; Collomb M-N; Neese F; DeBeer S Manganese K-Edge X-Ray Absorption Spectroscopy as a Probe of the Metal–Ligand Interactions in Coordination Compounds. Inorg. Chem 2012, 51, 680–687. [PubMed: 22145735]

(139). Khedkar A; Roemelt M Active Space Selection Based on Natural Orbital Occupation Numbers from n-Electron Valence Perturbation Theory. J. Chem. Theory Comput 2019, 15, 3522–3536. [PubMed: 31059643]

(140). Khedkar A; Roemelt M Extending the ASS1ST Active Space Selection Scheme to Large Molecules and Excited States. J. Chem. Theory Comput 2020, 16, 4993–5005. [PubMed: 32644789]

(141). Angeli C; Cimiraglia R; Evangelisti S; Leininger T; Malrieu J Introduction of n-Electron Valence States for Multireference Perturbation Theory. J. Chem. Phys 2001, 114, 10252–10264.

(142). Ganyushin D; Neese F First-Principles Calculations of Zero-Field Splitting Parameters. J. Chem. Phys 2006, 125, No. 024103.

(143). Hess BA; Marian CM; Wahlgren U; Gropen O A Mean-Field Spin-Orbit Method Applicable to Correlated Wavefunctions. Chem. Phys. Lett 1996, 251, 365–371.

(144). Neese F Efficient and Accurate Approximations to the Molecular Spin-Orbit Coupling Operator and Their Use in Molecular g-Tensor Calculations. J. Chem. Phys 2005, 122, No. 034107.

(145). Gerloch M; McMeeking R Paramagnetic Properties of Unsymmetrical Transition-Metal Complexes. J. Chem. Soc., Dalton Trans 1975, 2443–2451.

(146). Bolvin H An Alternative Approach to the g-Matrix: Theory and Applications. ChemPhysChem 2006, 7, 1575–1589. [PubMed: 16810728]

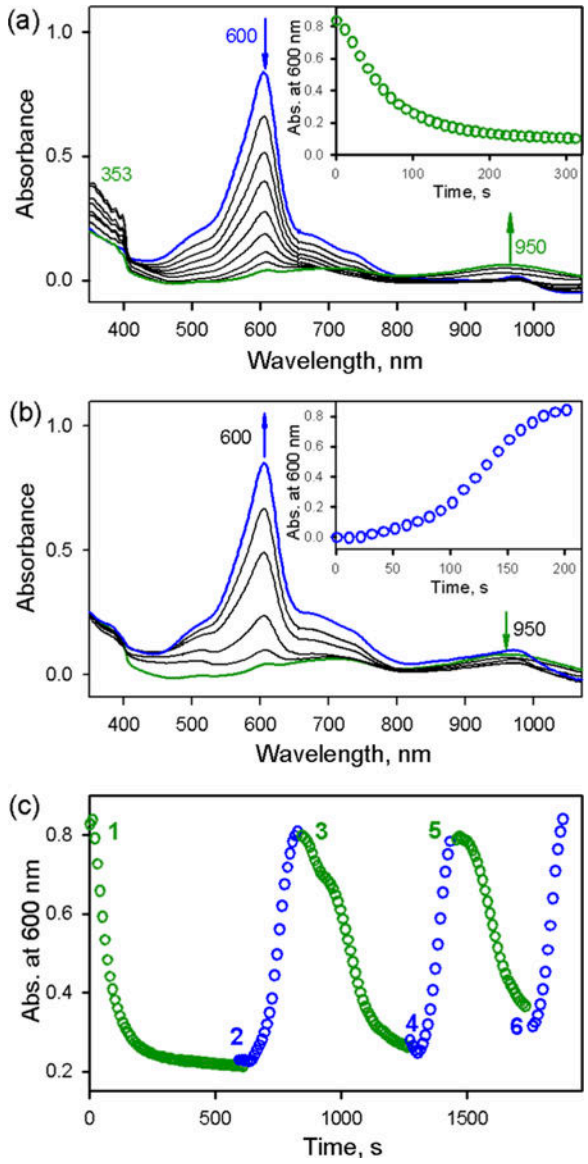

Figure 1.

UV-vis spectral changes showing the conversion of **1** (blue line) to **2** (green line) and vice versa by changing the reaction temperatures from (a) 253 K to 193 K (inset: 600 nm, green circles) and (b) 193 K to 253 K (inset: 600 nm, blue circles). The sigmoidal time trace in inset is due to the time for increasing the solution temperature. (c) Reversible spectral changes in the time course monitored at 600 nm by changing the reaction temperature from 253 K to 193 K (1, 3, and 5; green circles) and 193 K to 253 K (2, 4, and 6; blue circles). Intermediate **1** was generated by adding PhIO (3.0 equiv) and HOTf (5.0 equiv) to $[(TAML)Co^{III}]^{-}$ (0.10 mM) in acetone at 253 K.

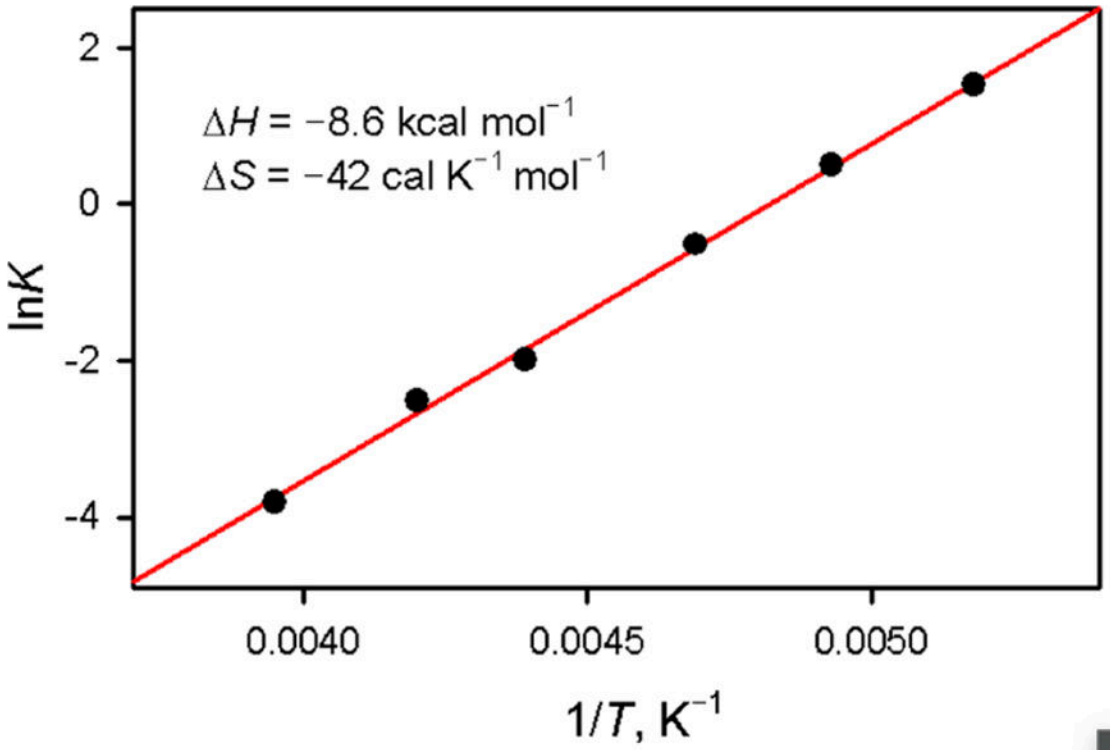

Figure 2.

A van't Hoff plot of the equilibrium constant between **1** and **2** in the presence of HOTf in acetone. Intermediates **1** was generated by the addition of HOTf (5.0 equiv.) to a reaction mixture of Li[(TAML)Co^{III}].3H_2O (0.20 mM) and PhIO (3.0 equiv.) in acetone at 253 K.

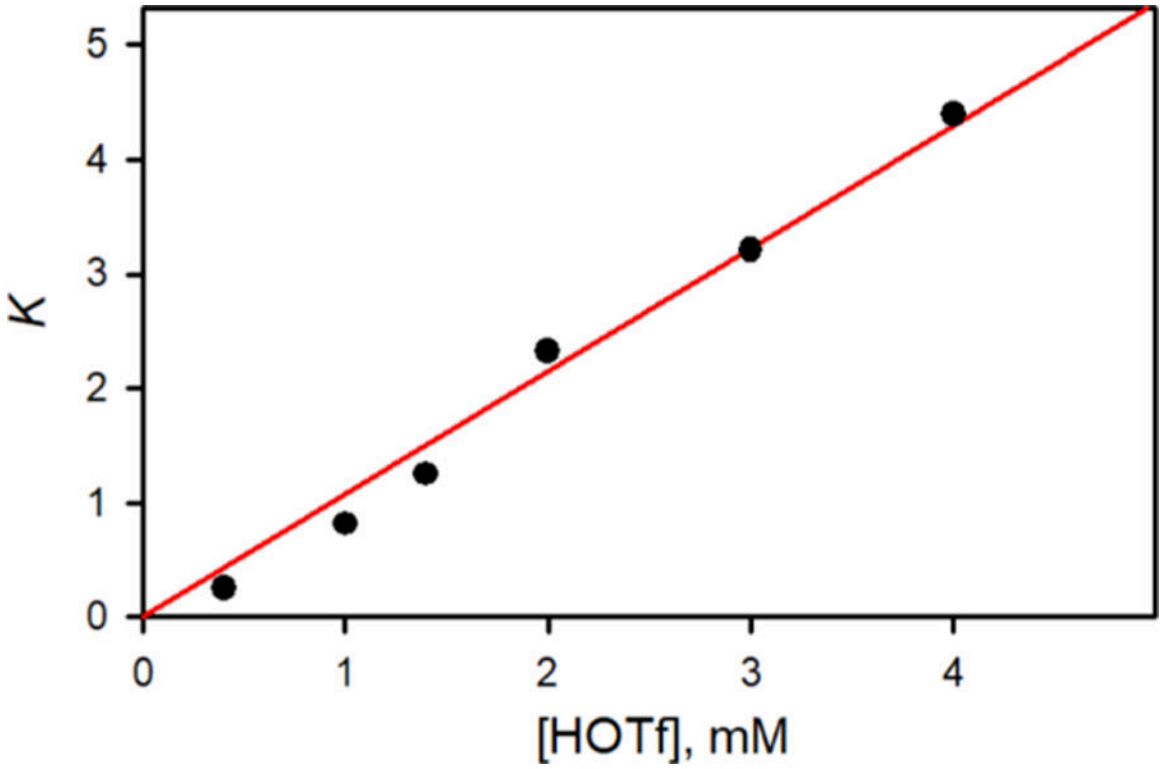

Figure 3.

Plot of *K* for interconversion between **1** and **2** vs concentration of HOTf in acetone at 233 K. Intermediates **1** was generated by the addition of HOTf (0.40 – 4.0 mM) to a reaction mixture of Li[(TAML)Co^{III}]•$3H_2O$ (0.20 mM) and PhIO (0.60 mM) in acetone at 253 K.

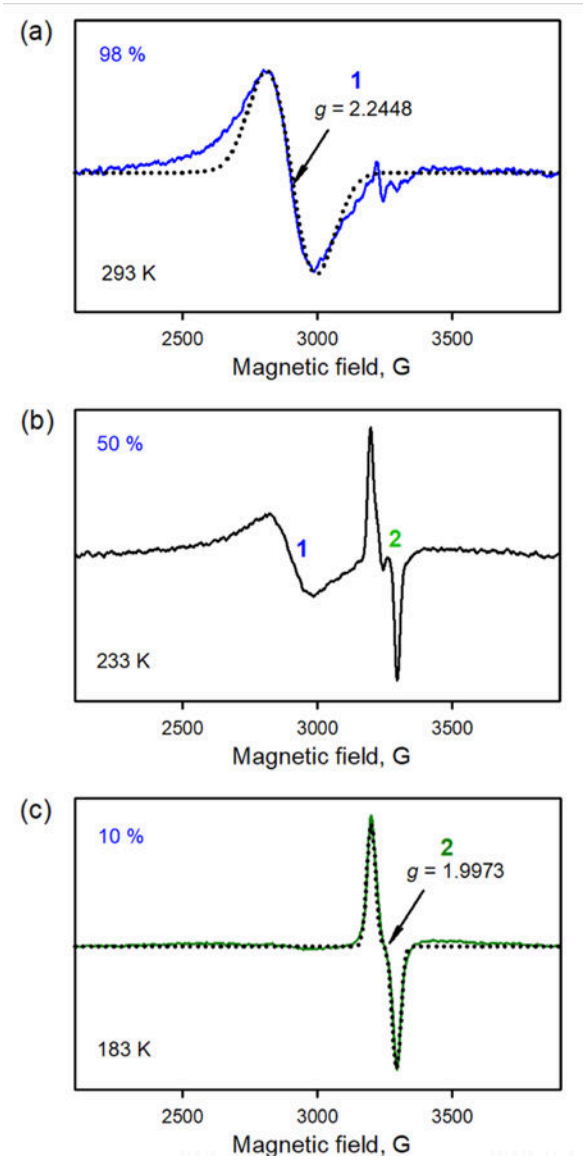

Figure 4.

Solution EPR spectra of **1** and **2** obtained in the reaction of $[(TAML)Co^{III}]^{-}$ (4.0 mM) and PhIO (3.0 equiv) in the presence of HOTf (5.0 equiv) in acetone at (a) 273 K, (b) 233 K, and (c) 193 K. Black dotted lines in (a) and (c) show the simulated spectra with simulation parameters of g_{avg} = 2.2449 and A_{avg} = 24 MHz for **1** and g_{avg} = 1.9973 and A_{avg} = 28 MHz for **2**.

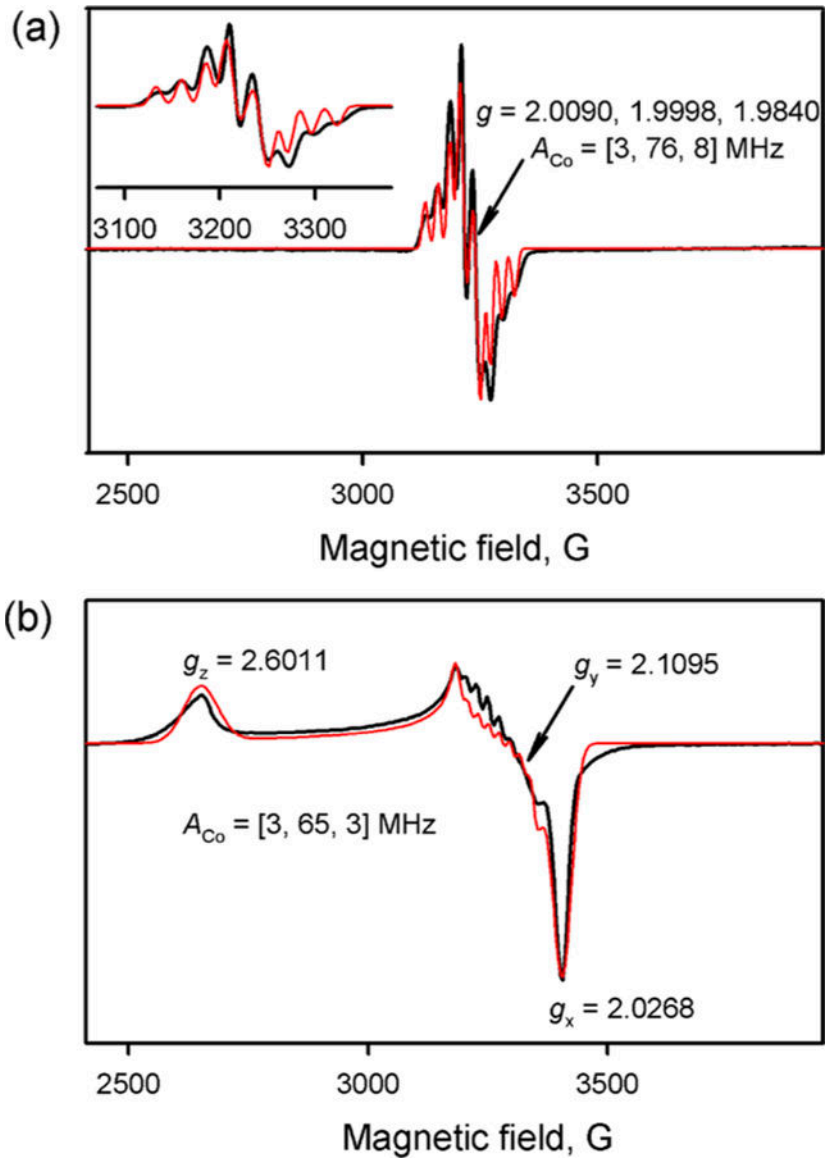

Figure 5.

X-band CW-EPR spectra of (a) **2** (black line) produced in the reaction of $[(TAML)Co^{III}]^{-}$ (1.0 mM) and PhIO (3.0 equiv) in the presence of HOTf (5.0 equiv) in acetone at 193 K (inset shows an expansion of the 3100–3300 G region) and (b) **1** (black line) produced in the reaction of $[(TAML)Co^{III}]^{-}$ (1.0 mM) and PhIO (3.0 equiv) in the presence of $Y(OTf)_3$ (2.0 equiv) in TFE/acetone (*v*/*v* = 19:1) at 253 K. EPR spectra were recorded at 5 K. Red lines show the simulated spectra.

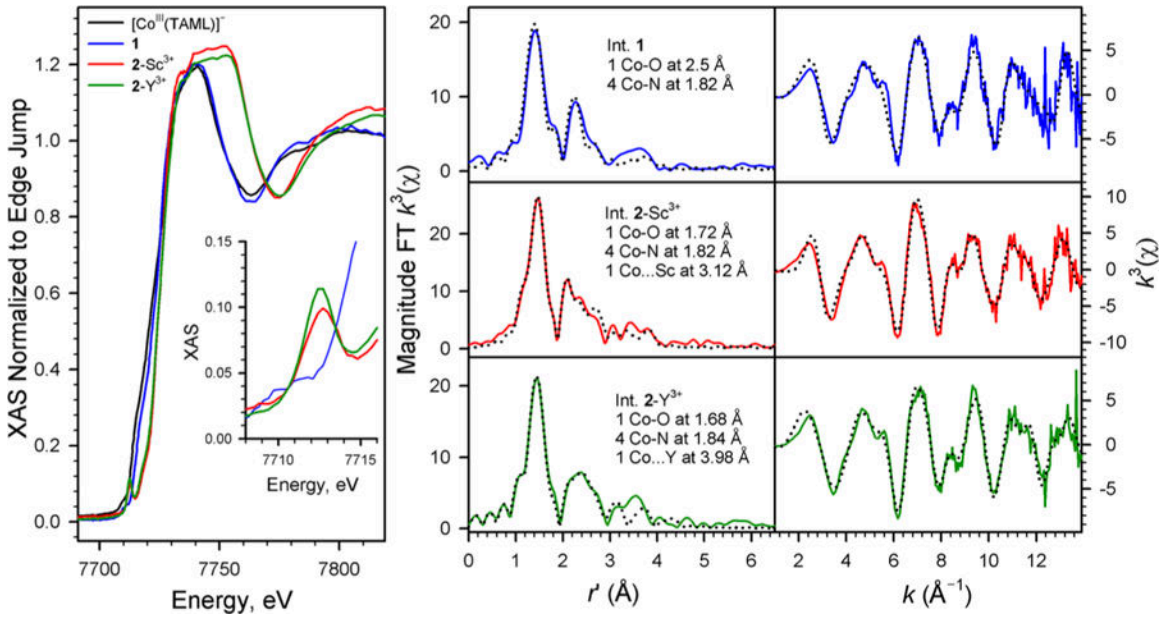

Figure 6.

Left: Edge-region of the cobalt K-edge X-ray absorption spectra of $[(TAML)Co^{III}]^{-}$ (black spectrum), **1** (blue spectrum), and **2** with $Sc(OTf)_3$ (**2**-Sc^{3+}, red spectrum) and **2** with $Y(OTf)_3$ (**2**-Y^{3+}, green spectrum). The inset depicts the pre-edge peak corresponding to the nominal Co(1s → 3d) transition of **1** and **2**. Right: The magnitude k^3 FT and unfiltered k^3 EXAFS spectra of **1** (top), **2**-Sc^{3+} (middle), and **2**-Y^{3+} (bottom). The experimental data are depicted as the red solid lines and the best fit to the experimental data are depicted as the dashed black lines.

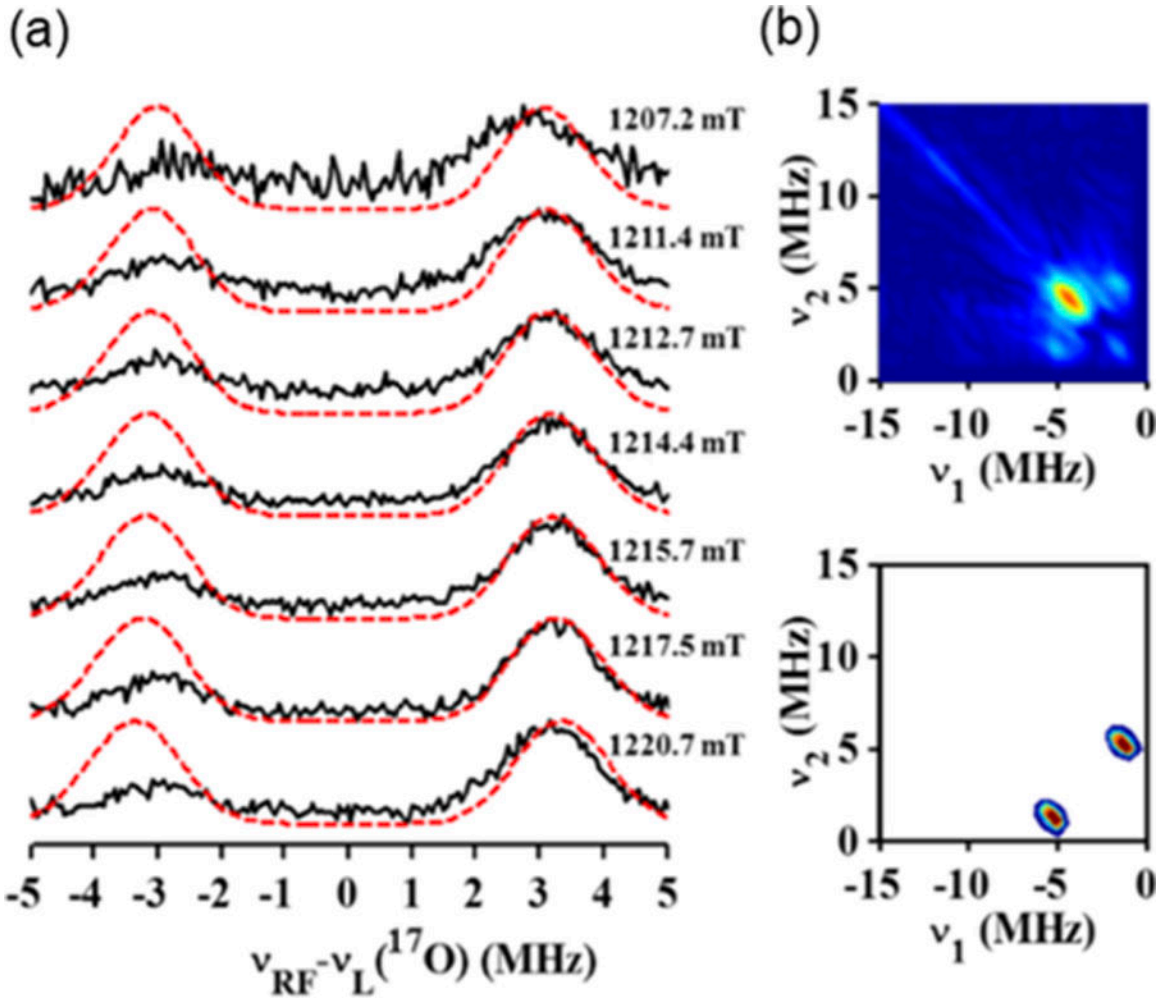

Figure 7.

(a) 34 GHz ^{17}O Davies ENDOR spectra of **2** (solid black lines) and its simulated spectra (dashed red lines). (b) 9 GHz HYSCORE spectrum (upper) and its simulation (lower).

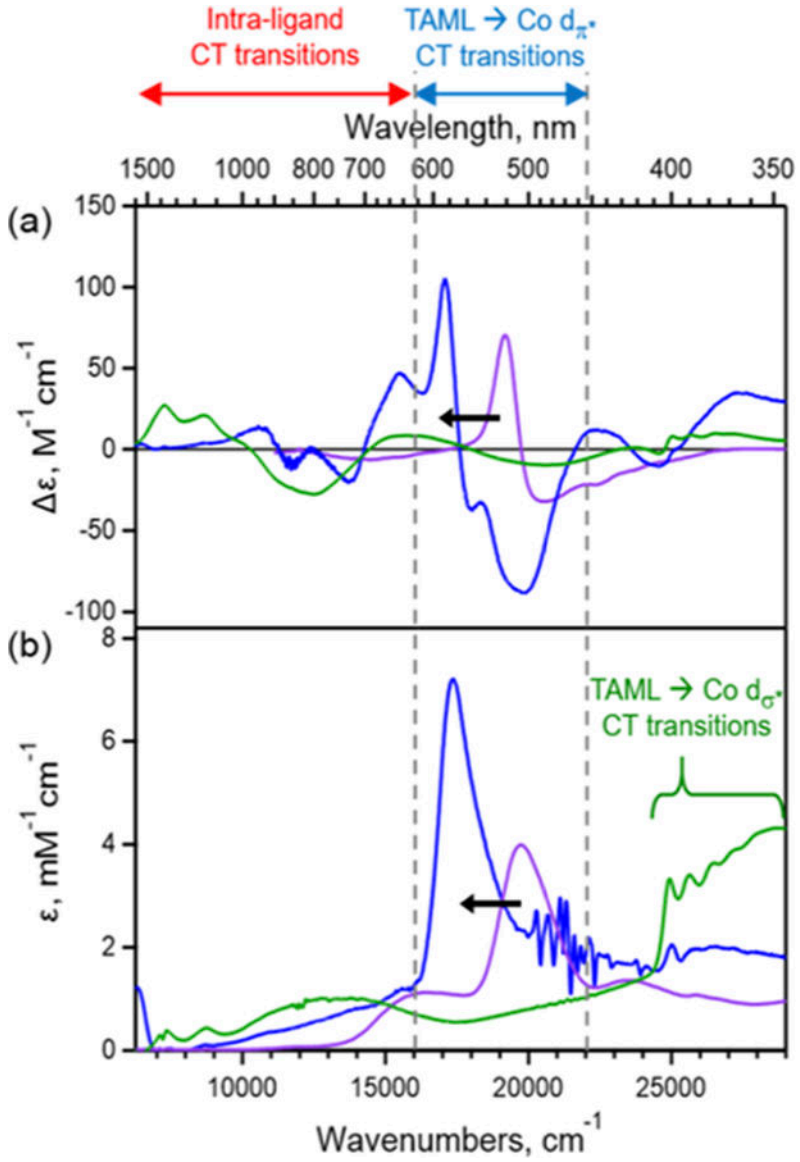

Figure 8.

(a) 7 T magnetic circular dichroism and (b) electronic absorption spectra of [(TAML)Co^{III}]$^{-}$ (purple) in butyronitrile at 40 K, **1** (blue) in TFE/acetone (*v/v* = 19:1) at 5 K, and **2** (green) in a mixed solvent of acetone/toluene (*v/v* = 1:2) at 5 K.

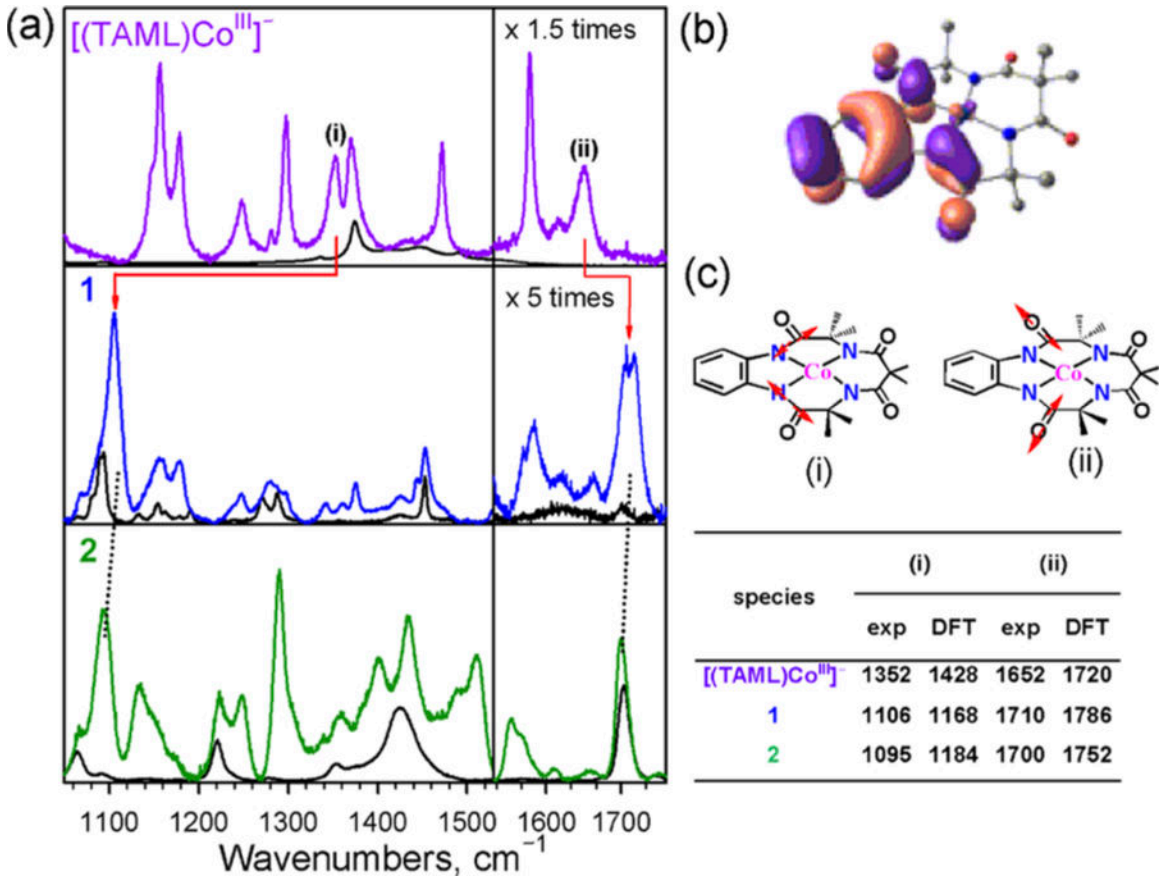

species	(i)		(ii)	
	exp	DFT	exp	DFT
[(TAML)Co^{III}]$^-$	1352	1428	1652	1720
1	1106	1168	1710	1786
2	1095	1184	1700	1752

Figure 9.

(a) rRaman spectra of [(TAML)Co^{III}]$^-$ in acetonitrile at room temperature obtained with 532-nm laser excitation (top), **1** in TFE/acetone (*v*/*v* = 19:1) at 233 K obtained with 532 nm laser excitation (middle), and **2** in acetone at 193 K obtained with 830 nm (bottom left) and 633 nm (bottom right) laser excitation. Features from solvents are presented in black lines. (b) HOMO of [(TAML)Co^{III}]$^-$, which becomes SOMO upon oxidation to **1** and **2**. (c) DFT-calculated normal modes corresponding to the Raman features (i) and (ii). Experimental and DFT-calculated frequencies are given in cm^{-1}.

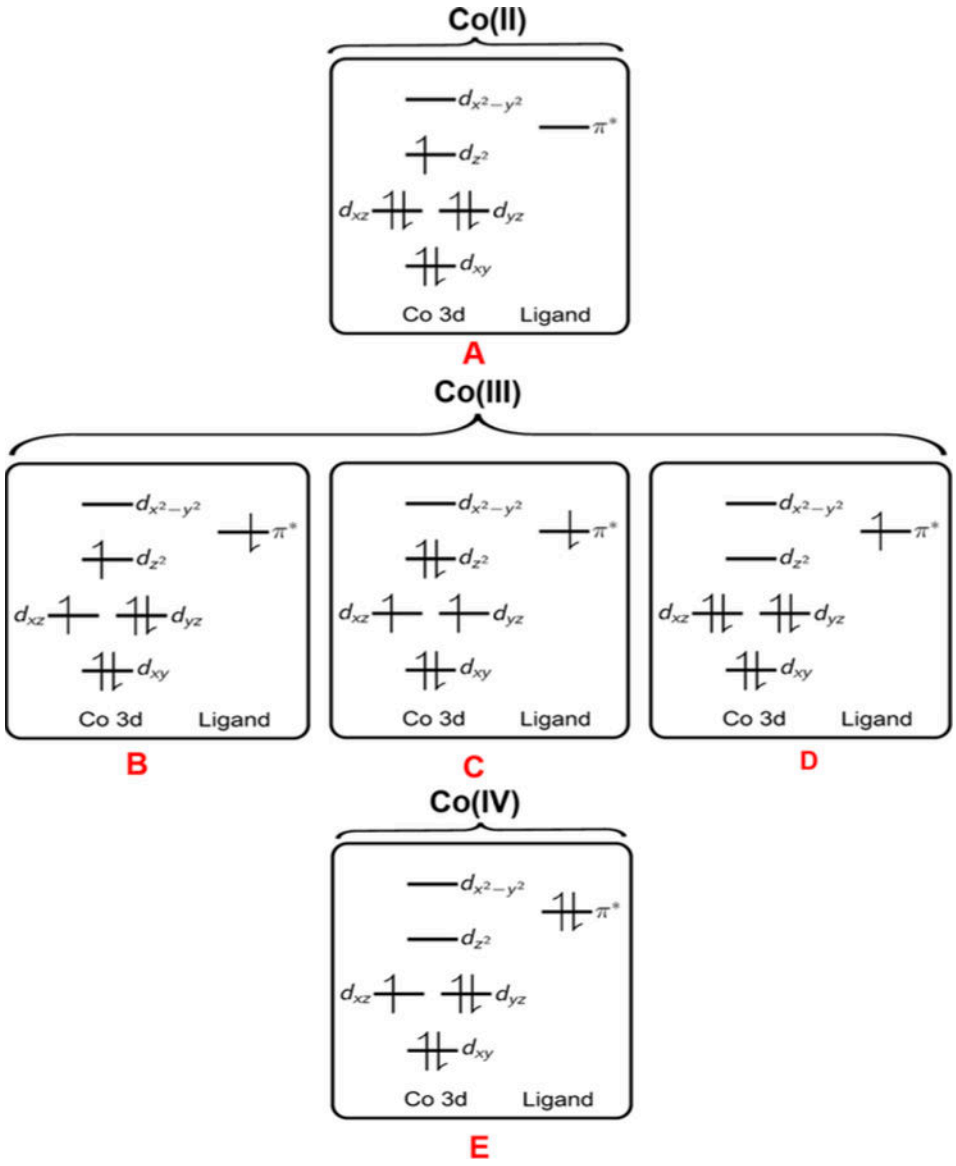

Figure 10.

Important configurations for the discussion of the electronic ground states of **1** and **2**. The electronic ground state of **1** and its spectroscopic properties are dominated by configurations **B** and **C**. In contrast, configurations **D** and **E** are most prominent in the electronic ground state of **2**. Note that the configurations with a hole in d_{yz} rather than d_{xz} are degenerate with **B** and **E**.

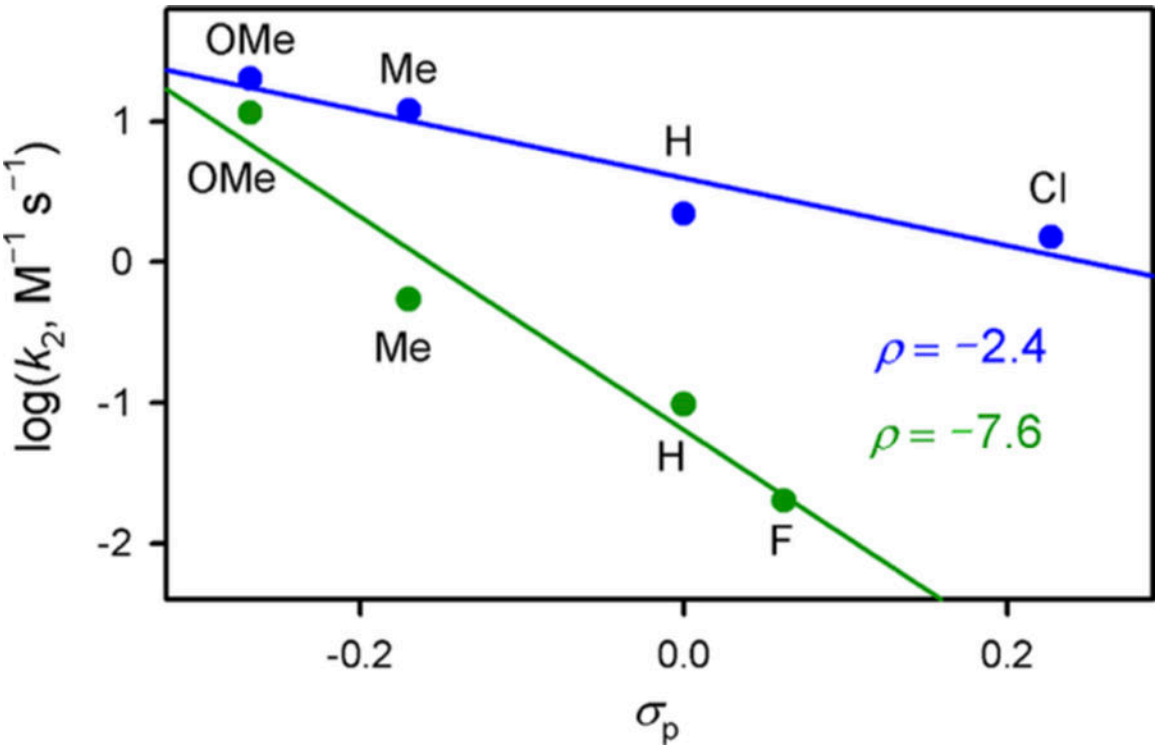

Figure 11.

Hammett plots of log k_2 against σ_p values of *para*-substituents of thioanisole derivatives for sulfoxidation of *para*-X-substituted thioanisoles, *p*-X-$C_6H_4SCH_3$ (X = OMe, Me, H, F, and Cl), by **1** (blue trace) and **2** (green trace) in acetone at 233 K.

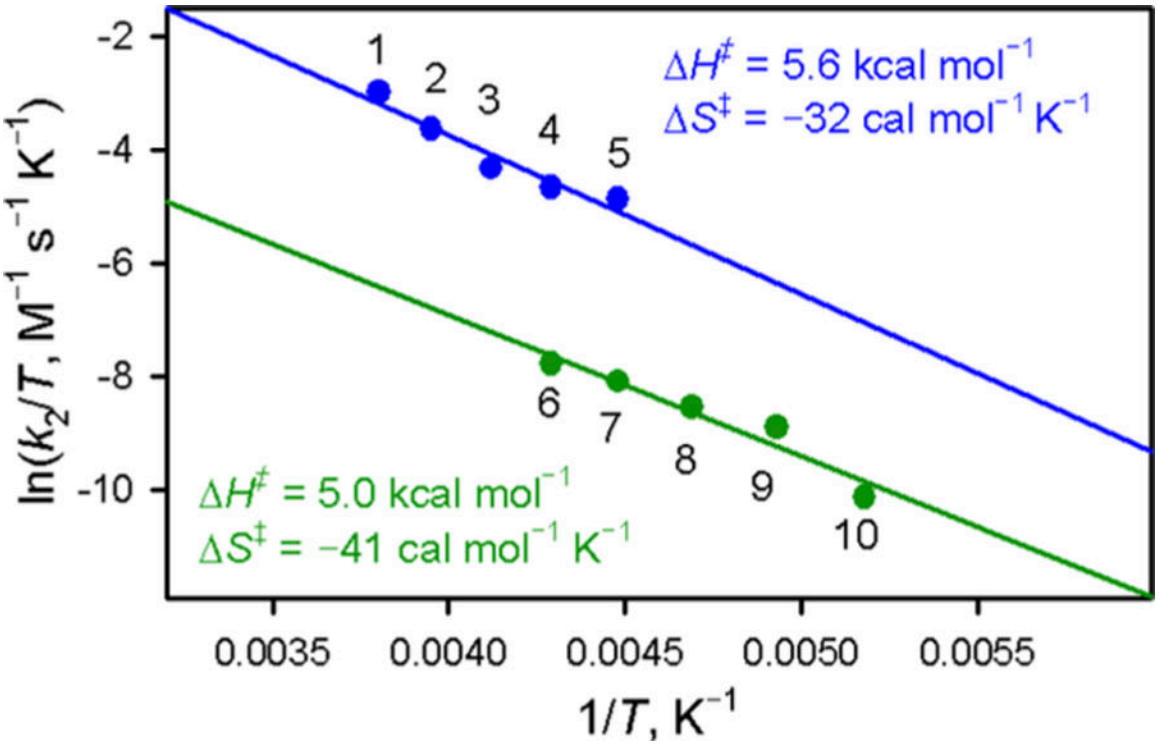

Figure 12.

Eyring plots of the rate constants (k_2) of oxygen atom transfer (OAT) from thioanisole to **1** in acetone at various temperatures [blue circles: (1) 263 K, (2) 253 K, (3) 243 K, (4) 233 K, and (5) 223 K] and OAT from thioanisole to **2** in acetone at various temperatures [green circles: (6) 233 K, (7) 223 K, (8) 213 K, (9) 203 K, and (10) 193 K].

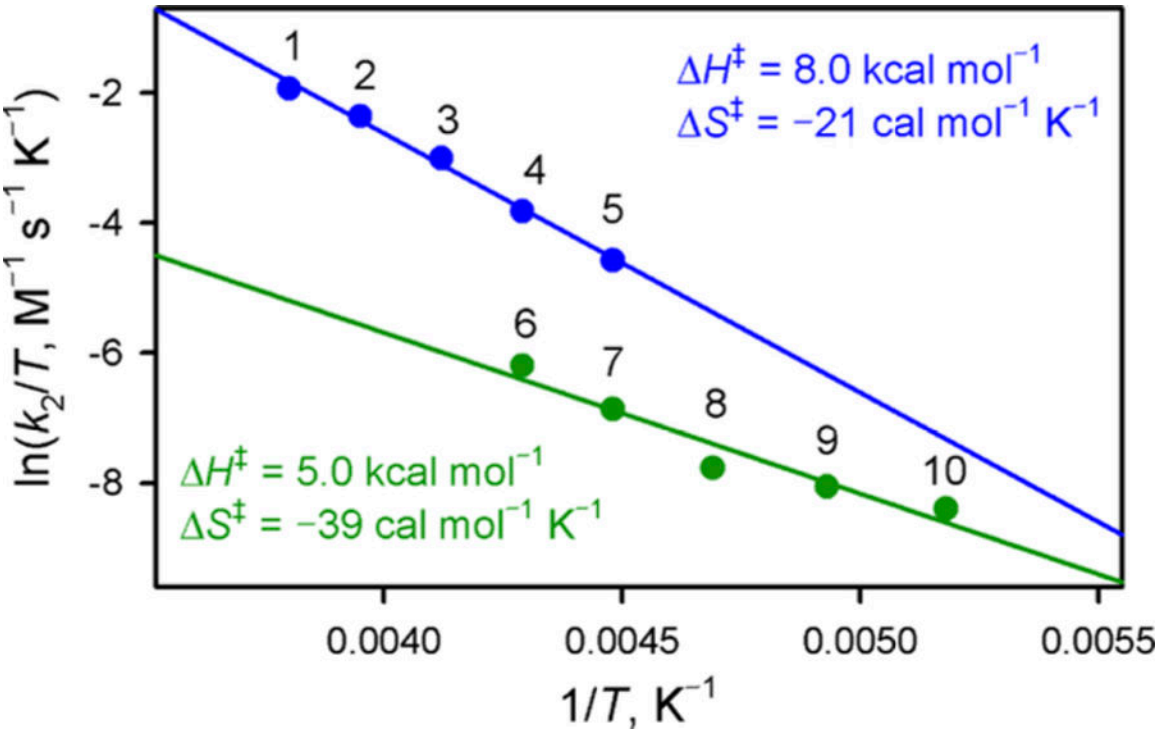

Figure 13.

Eyring plots of the rate constants (k_2) of O-H bond activation from 2,6-di-*tert*-butylphenol (2,6-DTBP) to **1** in acetone at various temperatures [blue circles: (1) 263 K, (2) 253 K, (3) 243 K, (4) 233 K, and (5) 223 K] and O-H bond activation from 2,6-DTBP to **2** in acetone at various temperatures [green circles: (6) 233 K, (7) 223 K, (8) 213 K, (9) 203 K, and (10) 193 K].

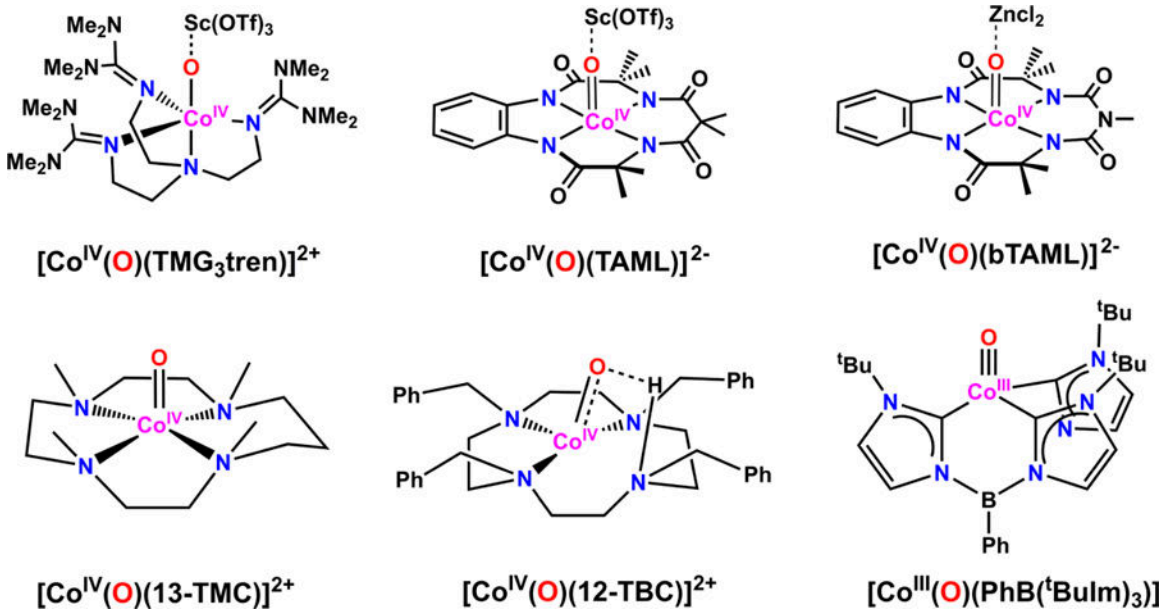

Scheme 1.
Molecular Structures of Reported Cobalt-Oxo Complexes

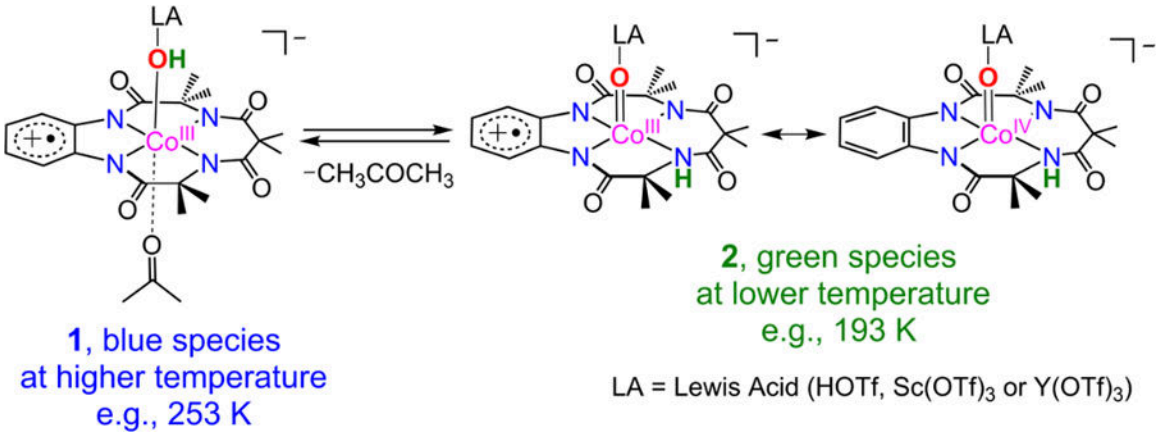

Scheme 2.

Proposed Structures of Intermediates 1 and 2 and Their Equilibrium Depending on Reaction Temperatures

Table 1.

Important Contributions (> 20%) to the Electronic Ground States of **1** and **2** (see Figure 10) and g_{iso} Values as Predicted by NEVPT2(13,9) Calculations

	***d*(Co-O)** [a]	**contribution** [b]	g_{iso}
1 (5-coord)	2.40 Å	78 % C	2.00
1 (6-coord)	2.50 Å	28 % A, 29 % B, 20 % C	2.41
2	1.85 Å	25% D, 20% E	2.08

[a] A more extensive data set is given in the Supporting Information.

[b] The missing contributions comprise configurations **A**-**E** as well as other excited configurations.